Journal of Geodesy (2025) 99:33
https://doi.org/10.1007/s00190-025-01957-3

ORIGINAL ARTICLE

3D high-resolution numerical modelling of altimetry-derived marine gravity data

Róbert Čunderlík[1] · Marek Macák[1] · Michal Kollár[1] · Zuzana Minarechová[1] · Karol Mikula[1]

Received: 5 July 2023 / Accepted: 25 March 2025 / Published online: 26 April 2025

Abstract
The paper presents 3D numerical modelling of the altimetry-derived marine gravity data with the high horizontal resolution 1×1 arc min. The finite volume method (FVM) as a numerical method is used to solve the altimetry–gravimetry boundary-value problem. Large-scale parallel computations result in the disturbing potential in every finite volume of the discretized 3D computational domain between an ellipsoidal approximation of the Earth's surface and an upper boundary chosen at altitude of 200 km. Afterwards, the first, second or higher derivatives of the disturbing potential in different directions can be numerically derived using the finite differences. A crucial impact on achieved accuracy has the process of preparing the Dirichlet boundary conditions over oceans/seas. It is based on nonlinear filtering of the geopotential generated on a mean sea surface (MSS) from a GRACE/GOCE-based satellite-only global geopotential model. The paper presents different types of the altimetry-derived marine gravity data obtained on the DTU21_MSS as well as at higher altitudes of the 3D computational domain. The altimetry-derived gravity disturbances on the DTU21_MSS are compared with those from recent datasets like DTU21_GRAV or SS_v31.1. Standard deviations of the residuals are about 2.7 and 2.9 mGal, respectively. The obtained altimetry-derived gravity disturbances at higher altitudes are compared with airborne gravity data from the GRAV-D campaign in US showing accuracy about 3 mGal. In addition, the gravity disturbing gradients as the second derivatives or the third derivatives are provided with the same high resolution on the DTU21_MSS as well as at different altitudes.

Keywords Altimetry-derived marine gravity data · High-resolution global gravity field modelling · Altimetry-gravimetry boundary-value problem · Finite volume method (FVM) · Numerical solution · Large-scale parallel computations

1 Introduction

A progress of satellite radar altimetry over the last three decades has significantly contributed in the fields of oceanography, hydrology, geodesy and cryospheric sciences (International Altimetry Team 2021). Huge amount of altimetric observation collected over more than 30 years has resulted in mean sea surface (MSS) models whose accuracy is nowadays about a few centimetres and are provided in the high-resolution 1×1 arc min, e.g. the recent ones DTU21_MSS (Andersen et al. 2021) or MSS_CNES_CLS2022 (Schaeffer et al. 2023). New altimetric data are still improving detailed information about the MSS undulation which also contributes to a recovery of the marine gravity field.

There have been many studies and research groups dealing with deriving the global or local marine gravity field from altimetry. A worthwhile overview of developed methods and provided data series can be found in Li et al. (2021). In this

✉ Róbert Čunderlík
robert.cunderlik@stuba.sk

Marek Macák
marek.macak@stuba.sk

Michal Kollár
michal.kollar@stuba.sk

Zuzana Minarechová
zuzana.minarechova@stuba.sk

Karol Mikula
karol.mikula@stuba.sk

[1] Department of Mathematics and Descriptive Geometry, Faculty of Civil Engineering, Slovak University of Technology, Radlinského 11, 810 05 Bratislava, Slovakia

paper, we mention two main research groups that are continuously (more than 2 decades) providing and updating their global altimetry-derived marine gravity field models, namely, the 'S&S' series from the Scripps Institution of Oceanography, University of California San Diego (SIO), and 'DTU' series from the Technical University of Denmark (DTU).

The S&S approach is based on processing the sea surface slopes that correspond to deflections of the vertical, and the altimetry-derived gravity anomalies are calculated using the inverse Vening-Meinesz formula (see Sandwell and Smith 1997, 2009; Hwang and Parsons 1996; Hwang 1998; Sandwell et al. 2014, 2021). The DTU approach is based on processing the sea surface heights that correspond to the geoid undulation, and the altimetry-derived gravity anomalies are modelled using the inverse Stokes formula (see Andersen and Knudsen 1998, 2016, 2020; Andersen et al. 2010, 2014). In principle, both approaches utilize geometrical information about the marine geoid that is obtained from the MSS by subtracting some a-priori known mean dynamic topography (MDT).

Our approach to recover the marine gravity data from altimetry is based on a numerical solution of the altimetry-gravimetry boundary-value problem (AGBVP) using the finite volume method (FVM). In the past, many researchers have been dealing with AGBVP, mostly from the theoretical point of view (see, e.g. Mather 1974; Holota 1980, 1983a,b; Sansó 1983; Svensson 1983; Bjerhammar and Svensson 1983; Sacerdote and Sansó 1987; Lehmann 1999, 2000; or Grebenitcharsky and Sideris 2005), while defining three types of AGBVP according to the type of input data. In this paper, we focus on practical aspects of the high-resolution numerical solution of AGBVP, namely the AGBVP of the third type (AGBVP-III), where the ellipsoidal heights of the sea surface topography are known (see, e.g. Lehmann 1999 or Čunderlík and Mikula 2009).

A key idea of our approach is that the precise 3D position of MSS in combination with some GRACE/GOCE-based satellite-only global geopotential model (GGM) provides the Dirichlet boundary condition (BC) over oceans/seas for solving AGBVP-III. Such a treatment gives to our approach more physical meaning. In addition, no a-priori MDT model is needed to get our input data. Instead, the geopotential evaluated on the MSS model has to be appropriately filtered in order to reduce typical noise for spherical harmonics (SH) approaches as a drawback of the omission errors of the SH-based satellite-only GGMs. Hence, the filtered geopotential on MSS, from which the Dirichlet BC is computed, already includes information about the MDT. Moreover, this combination results in the high-frequency information about the gravity field over oceans/seas despite the fact that the satellite-only GGMs contains only its low- or medium-frequency part. This is crucial in our approach while accuracy of such Dirichlet BC as input data is essential for our numerical modelling.

The FVM approach solves the AGBVP-III in the 3D computational domain between an ellipsoidal approximation of the Earth's surface and an upper boundary chosen at the altitude of 200 km. On this upper boundary, the FVM solution is fixed to the disturbing potential generated from the satellite-only GGM. It aims to utilize information about the Earth's gravity field detected by the gravity satellite missions at altitudes of their observations. Taking into account that the FVM approach is solving the AGBVP-III in spatial domain, smoother low-frequency information on the upper boundary and detailed high-frequency information on the bottom boundary represent BCs that should correspond to real behaviour of the gravity field considered in spatial domain. Then, our FVM numerical solution of the Laplace equation can be interpreted as a 3D physics-based interpolation of the gravity field information from these two boundaries into the 3D space between them.

In our approach, the 3D computational domain is discretized with the high horizontal resolution 1×1 arc min and with a non-uniform division in the radial direction. It leads to large-scale parallel computations with large memory requirements. The FVM numerical solution results in the disturbing potential obtained in the whole 3D computational domain with high resolution. Afterwards, the altimetry-derived gravity data can be numerically derived as the first, second or higher derivatives in different directions using the finite differences.

The paper is structured as follows: Section 2 reminds a definition of the AGBVP-III and introduces its 'satellite-fixed' modification. Then, the FVM approach is very briefly mentioned without its mathematical background since it has been already published in our previous paper (Minarechová et al. 2015). Section 3 describes the 3D computational domain and its high-resolution discretization. Section 4 provides details about all the boundary conditions used as input data. Here, the crucial part is focused on a process of preparing the Dirichlet BC over oceans/seas that is based on nonlinear filtering of the geopotential on MSS. Then, Sect. 5 summarizes computational aspects of the final large-scale parallel computations. Section 6 presents the obtained altimetry-derived marine gravity data. The gravity disturbances on the bottom boundary are compared with the recent datasets of the DTU approach and S&S approach, and all three datasets are tested by shipborne gravimetry. The gravity disturbances at higher altitudes are tested by airborne gravimetry from the GRAV-D campaign (Youngman et al. 2012) in coastline regions of USA. Section 7 discusses our conclusions and outlines some insights for further improvements.

2 Finite volume method for a numerical solution of the altimetry–gravimetry boundary-value problem

The linear AGBVP of the third type represents the scalar-fixed exterior BVP for the Laplace equation with the mixed BCs (see, e.g. Lehmann 1999),

$$\Delta T(\boldsymbol{x}) = 0, \quad \boldsymbol{x} \in R^3 - E, \tag{1}$$

$$T(\boldsymbol{x}) = T^{\mathrm{MSS}}(\boldsymbol{x}), \quad \boldsymbol{x} \in \Gamma_{\mathrm{Sea}}, \tag{2}$$

$$\langle \nabla T(\boldsymbol{x}),\ \boldsymbol{s}(\boldsymbol{x}) \rangle = -dg(\boldsymbol{x}),\ \boldsymbol{x} \in \Gamma_{\mathrm{Land}}, \tag{3}$$

$$T = O\left(|\boldsymbol{x}|^{-1}\right) \text{ as } \boldsymbol{x} \to \infty, \tag{4}$$

where T is the disturbing potential defined as a difference between the geopotential W and normal gravity potential U at any point $\boldsymbol{x}$, the domain E is the body of the Earth with its boundary $\Gamma = \Gamma_{\mathrm{Sea}} \cup \Gamma_{\mathrm{Land}}$ (the Earth's surface) (Fig. 1a) and $\langle , \rangle$ stands for the inner product of two vectors. T^{MSS} represents the Dirichlet BC in the form of the disturbing potential prescribed on MSS (Sect. 4 describes all details how to get this kind of input data). The surface gravity disturbance $\delta g(\boldsymbol{x})$ as input data in Eq. (3) compares the magnitudes of the actual and normal gravity, i.e. $\delta g(\boldsymbol{x}) = g(\boldsymbol{x}) - \gamma(\boldsymbol{x}) = |\nabla W(\boldsymbol{x})| - |\nabla U(\boldsymbol{x})|$. It represents the oblique derivative BC since the normal to the Earth's surface Γ does not coincide with the vector $\boldsymbol{s}(\boldsymbol{x}) = -\nabla U(\boldsymbol{x})/|\nabla U(\boldsymbol{x})|$ (the surface deflection of the vertical is neglected). Equation (4) represents a condition of the regularity of the disturbing potential at infinity.

Although AGBVP in Eqs. (1)–(4) is defined for the infinity domain $R^3 - E$, in our approach we restrict this infinite domain above the Earth's surface into a finite domain Ω, which is bounded by an artificial upper boundary Γ_{SAT} chosen approximately at altitude of the GOCE satellite orbits (Fig. 1a). Here we prescribe the Dirichlet BC in the form of the disturbing potential T^{SAT} generated from a satellite-only GGM

$$T(x) = T^{\mathrm{SAT}}(x), \quad x \in \Gamma_{\mathrm{SAT}}. \tag{5}$$

Consequently, we abandon a condition of the regularity at infinity from Eq. (4). Instead at infinity, the seeking solution of the Laplace Eq. (1) for $\boldsymbol{x} \in \Omega$ is fixed on the upper boundary Γ_{SAT} to a chosen GRACE/GOCE-based satellite-only GGM. In this way, we utilize information about the Earth's gravity field detected by the satellite missions, however, at altitudes of their observations. Such a modification of the original AGBVP we call the 'satellite-fixed' AGBVP.

To solve the satellite-fixed AGBVP numerically, we use the finite volume method. FVM is a numerical method of variational calculus that is based on a local conservation of numerical fluxes. At first, the computational domain is discretized by the finite volumes. Then, a weak formulation of the Laplace equation in every finite volume is obtained using the divergence theorem. In this way, the volume integrals are converted to the surface integrals where normal derivatives represent fluxes. The flux entering a given volume is identical to that leaving the adjacent volume; thus, the FVM is conservative. The fluxes are approximated numerically yielding the so-called transmissivity coefficients (see Eymard et al. 2000).

Our choice to use FVM instead of the finite element method (FEM) (Reddy 2006), which is often a preferred numerical method, is simply based on lower memory requirements. FEM gives a numerical scheme with the 27-point stencil for hexagonal elements with linear basis functions, while our FVM implementation gives the 7-point stencil for hexagonal elements with constant basis functions. Hence, FVM leads to much sparser structure of matrix coefficients yielding 3–4 times lower memory requirements for large-scale computations. Consequently, it allows us to perform a more detailed discretization using the FVM mesh in comparison with the FEM mesh with the same memory costs. Since both FEM and FVM are second-order accurate methods, the lower memory requirements represent a preferred advantage of FVM in our application.

FVM as a numerical method requires a discretization of the computational domain Ω into finite volumes (Fig. 1b). Since our main objective is to determine altimetry-derived gravity data over oceans/seas, we can consider an ellipsoidal approximation of the Earth's surface Γ. Hence, the oblique derivative problem on lands Γ_{Land} in Eq. (3) will vanish and the input gravity disturbances will represent the Neumann BC. Over oceans/seas, the Dirichlet BC will be evaluated on MSS considering its precise 3D position (Sect. 4); however, in the FVM discretization, Γ_{Sea} will be approximated by the ellipsoidal surface. Such a simplification would not have a significant impact on accuracy of the altimetry-derived gravity data due to a property that FVM must satisfy the BC exactly, while the governing equation can be slightly relaxed (see Eymard et al. 2000).

To apply FVM to the satellite-fixed AGBVP, we use the same FVM numerical scheme as described in Minarechová et al. (2015), which has been developed to solve the fixed-gravimetric BVP. The only difference is that now the Dirichlet BC is considered over oceans/seas but numerically treated in the same way as the Dirichlet BC on the upper boundary. Therefore, the readers are kindly referred to Minarechová et al. (2015) where they can find all mathematical details about our FVM approach including its parallel implementation. In this paper, we rather focus on modelling

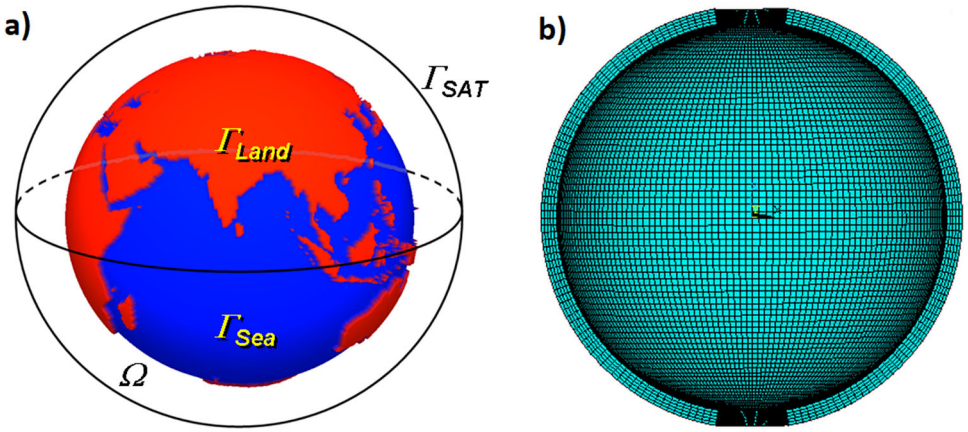

Fig. 1 An illustration of the computational domain Ω and its discretization

the high-resolution altimetry-derived gravity data and preparing the Dirichlet BC over oceans/seas, which is crucial in the whole process.

3 Discretization of the 3D computational domain

The 3D computational domain Ω bounded by the ellipsoidal approximation of the Earth's surface Γ and the artificial upper boundary Γ_{SAT} is discretized into the 3D mesh of finite volumes (Fig. 1b). Our aim is to reach the same high-resolution in the horizontal directions as the recent global MSS models are provided in, namely 1×1 arc min. In the radial direction, the domain Ω is discretized non-uniformly depending on altitude. The radial size of finite volumes of the first five 'layers' close to the reference ellipsoid is set to 50 m, so they are at the constant ellipsoidal heights of 0 m, 50 m, 100 m, 150 m and 200 m, respectively. From 200 m, the radial size of the finite volumes increases linearly with increasing altitude. For those on the upper boundary, it reaches 960 m. In this way, we can significantly reduce enormous memory requirements. To consider such a non-uniform division is quite natural taking into account that the gravity field becomes smoother and smoother with increasing altitude.

Finally, a number of the finite volumes in the radial direction (= number of 'layers') is set to 400. Hence, the 3D computational domain Ω consists of $21\,600 \times 10\,800 \times 400$ (longitude $\times$ latitude $\times$ height) $= 93\,312\,000\,000$ finite volumes/unknowns (233 280 000 unknowns on the reference ellipsoid). Our FVM approach applied on such a refined mesh would require about 4.9 TB of the internal memory. Since our cluster has only 1.5 TB, we are forced to apply the domain decomposition methods, namely the additive Schwarz method. It is based on splitting the whole computational domain into smaller subdomains that are slightly overlapped. Then, coefficients of the system matrix are always recomputed and stored just for one subdomain, while the linear system is solved separately on each subdomain. Appropriate overlapping of the subdomains enables to merge separate solutions on each subdomain into one global solution; for more details, see Macák et al. (2021). This process can significantly reduce enormous memory requirements, however, in the cost of much higher CPU time consumption (Sect. 5).

4 Boundary conditions as input data

The upper boundary Γ_{SAT} is chosen at the altitude of 200 km above the reference ellipsoid, which is slightly below the mean altitude of the GOCE orbits. It aims to partly reduce enormous memory requirements, while an impact on accuracy is negligible (Li et al. 2025). Here, the Dirichlet BC is prescribed in the form of the disturbing potential (Fig. 2). It is generated from the newest release of the GRACE/GOCE-based satellite-only GGM provided by ESA, namely from the GO_CONS_GCF_2_DIR_R6 model up to d/o 300 (Bruinsma et al. 2014).

On the bottom boundary, i.e. on the reference ellipsoid, we consider the mixed BCs. On lands/continents, the Neumann BC is considered in the form of gravity disturbances (Fig. 3) that are interpolated from the DTU15_GRAV dataset (Andersen and Knudsen 2016). On lands, such gravity data are based on the EGM2008 model up to d/o 2190 (Pavlis et al. 2012); however, the terrain effect evaluated from detailed digital terrain models is considered with the same high-resolution 1×1 arc min as the altimetry-derived data over oceans/seas.

Due to the ellipsoidal approximation of the Earth's surface, the oblique derivative problem vanishes. It is worth mentioning that the FVM solution computed on lands is of less importance in our case since this paper focuses on precise modelling of the altimetry-derived gravity data over oceans/seas. Therefore, we neither comment on quality of the input gravity disturbances on lands, nor we present or comment on the FVM solution obtained on lands. We rather

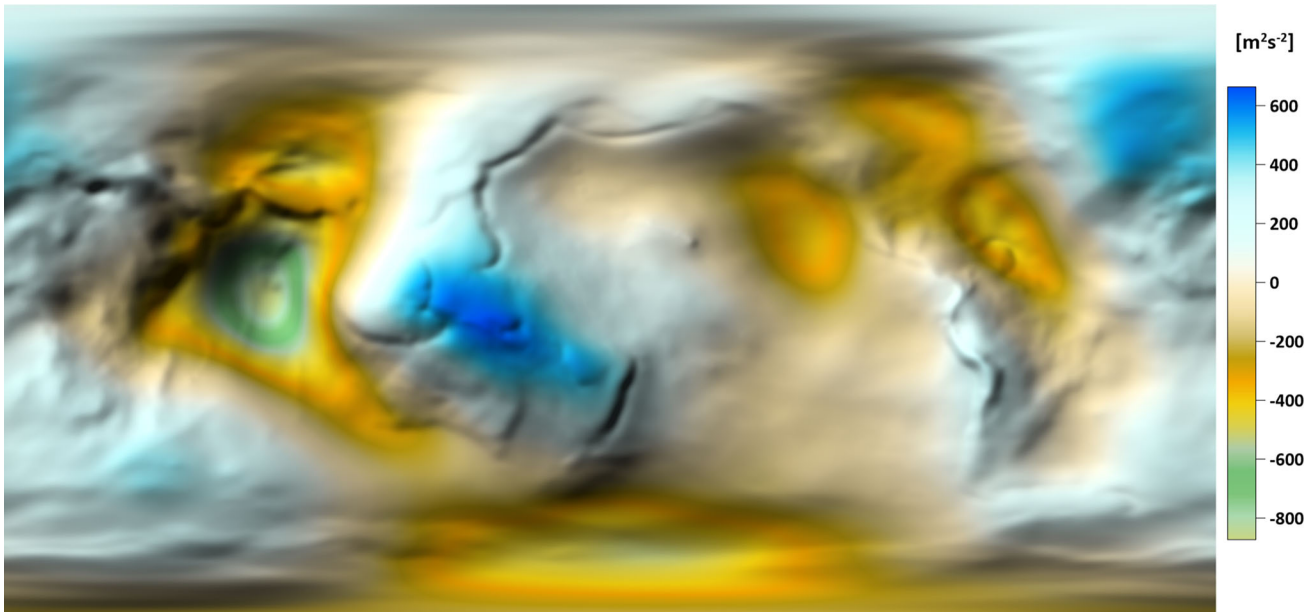

Fig. 2 The disturbing potential generated from the GO_CONS_GCF_2_DIR_R6 model as the Dirichlet boundary condition on the upper boundary 200 km above the reference ellipsoid

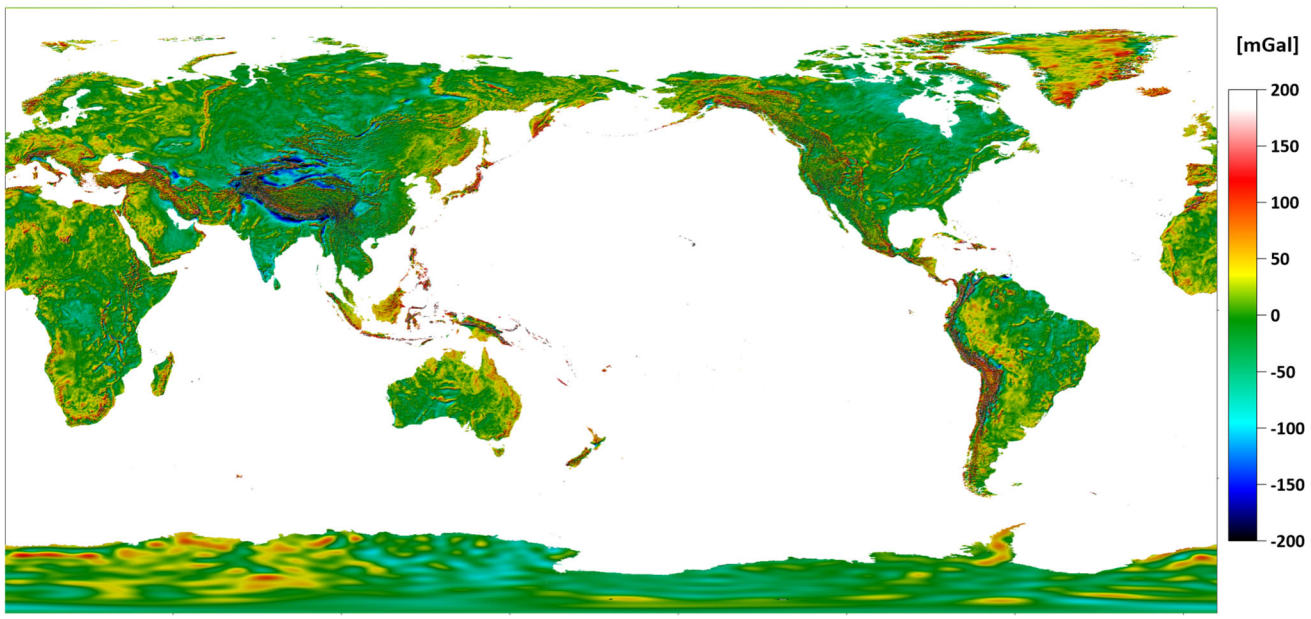

Fig. 3 The surface gravity disturbances on lands as the Neumann BC on the bottom boundary interpolated from the DTU15_GRAV dataset

focus on creating the Dirichlet BC over oceans/seas whose quality has a crucial impact on accuracy of the modelled altimetry-derived marine gravity data.

A key idea of our approach arises from a property that the geopotential on MSS should be a smooth function although the 'geometric shape' of MSS reflects all irregularities of the Earth's gravity field. Moreover, this geopotential on MSS should correspond to MDT expressed in potential units. The recent MSS models obtained from satellite altimetry provide precise high-frequency information about geometry of the sea level, which is induced by the gravity field, while the satellite-only GGMs provide precise low- or medium-frequency information about the gravity field. Their combination together with appropriate filtering in spatial domain can provide high-frequency information about the gravity field over oceans/seas despite the fact that they provide information in different spatial resolution.

In our experiments, we use the DTU21_MSS model in the high-resolution 1 × 1 arc min (Andersen et al. 2021). The geopotential W_i is generated from the GO_CONS_GCF_2_DIR_R6 model up to d/o 300 at all grid points of DTU21_MSS with its precise 3D positions. To reduce the SH-based noise, an appropriate filtering is inevitable. We can directly filter the geopotential W; however, just for a 'more convenient visualization', we transform the geopotential W into the MDT model using the expression

$$h_i^{MDT} = \frac{-(W_i - W_0)}{\gamma_i}, \tag{6}$$

where h^{MDT} is the ellipsoidal height of MDT at the grid point i, γ is the normal gravity which plays a role of the scaling factor, and $W_0 = 62{,}636{,}853.4\ \mathrm{m^2 s^{-2}}$ is a reference value of the geopotential on the geoid adopted for an establishment of the International Height Reference System (IHRS) (Sánchez et al. 2016). Such a treatment provides the satellite-only MDT model related to the adopted W_0 value, which avoids an issue of the zero-degree term of a chosen geoid model due to parameters of the normal gravity field.

Figure 4a depicts the obtained satellite-only MDT. To reduce the SH-based noise, we apply nonlinear diffusion filtering using the Perona–Malik model (Čunderlík et al. 2013). In this iterative process, diffusivity coefficients depend on an edge detector, which is updated at each iteration using gradients of the solution from the previous iterative step. It enables faster filtering in areas of small gradients and slower filtering in areas of high gradients. Such nonlinear filtering can efficiently reduce the noise while preserving important gradients along main ocean currents.

However, such a nonlinear filtering requires a special treatment in coastal areas, where information from the satellite-only MDT (Fig. 4a) has to be properly augmented to lands. This is quite a difficult task due to the fact that the SH-based noise can here reach amplitudes of several dm, especially along trenches close to coasts, while the important gradients along ocean currents are in the range of several cm. To treat this issue we use the following iterative procedure. In the first step, zero values are prescribed over lands and merged with the satellite-only MDT over oceans/seas. Such input data induces high gradients along coastlines; therefore, the linear diffusion, which corresponds to the Gaussian filtering, is firstly used as a pre-filtering. Then, the pre-filtered results over lands are removed and information from the obtained smooth MDT is augmented to lands by the 'nearest-neighbour' (NN) strategy for filling 'the missing data' using the Surfer® from Golden Software, LLC (www.goldensoftware.com).

In the second step, these augmented data over lands are merged with the original unfiltered satellite-only MDT over oceans/seas to provide new input data for filtering. Since the gradients along coastlines become much smaller, now the aforementioned nonlinear diffusion based on the Perona-Malik model can be already used. After nonlinear filtering, the results over lands are again removed and replaced by values augmented by NN from the new filtered MDT over oceans/seas. In the next steps, augmented data over lands are updated in every iteration, merged with original unfiltered satellite-only MDT and nonlinearly filtered. This iterative procedure is repeated until the values in coastal zones do not change significantly, i.e. changes are below a chosen criterion. In our case, we use 2 cm as a threshold. In this way, we can get the MDT values along coastlines without using any a-priori MDT model.

The last iteration of the nonlinear filtering leads to the final filtered MDT model (Fig. 4b). It can be used to derive velocities of the surface geostrophic currents (Fig. 4c) that can backwards validate the quality of our nonlinear filtering. To visually verify our results, the filtered MDT model is compared with (i) the DTU22_MDT model (Fig. 5a), which is the satellite-only MDT (Knudsen et al. 2022) derived from the same DTU21_MSS model, and (ii) with the MDT_CNES_CLS2022 model (Fig. 5b), which is the hybrid MDT (Jousset et al. 2022) derived from the MSS_CNES_CLS_15 (Pujol et al. 2018) and also includes information from drifters. These comparisons show large differences in polar regions, along main ocean currents and in coastal zones located close to trenches (e.g. in Philippines, Taiwan or Japan), which indicates problematic zones (more discussed in Sect. 6.1).

Afterwards, the filtered MDT model (Fig. 4b) is transformed back to the geopotential W using the relation from Eq. (6). It is worth noting that such a process yields exactly the same results as filtering directly the geopotential W. Finally, the normal potential U evaluated at all DTU21_MSS grid points is subtracted from the geopotential W resulting in the disturbing potential T^{MSS} as the Dirichlet BC in Eq. (2), see Fig. 6.

As mentioned above, the precision of the obtained Dirichlet BC is crucial for precision of the modelled altimetry-derived gravity data. Any noise in the prescribed disturbing potential over oceans/seas, even small, will be intensified in the derived quantities, i.e. in the first derivatives (gravity disturbances) and even more in the second derivatives (gravity disturbing gradients) or higher. To reduce such small noise that can be visible in the disturbing potential after detailed zooming, we again apply the nonlinear diffusion filtering; however, a combination of the Laplacian-influenced pre-filtering and the Perona–Malik model with the extreme detector (Čunderlík et al. 2016). At first, the pre-filtering reduces high amplitudes of the noise, and then, the nonlinear diffusion filtering is applied, where diffusivity coefficients depend on both, the edge detector as well as extreme detector. This combination allows us to remove small noise while

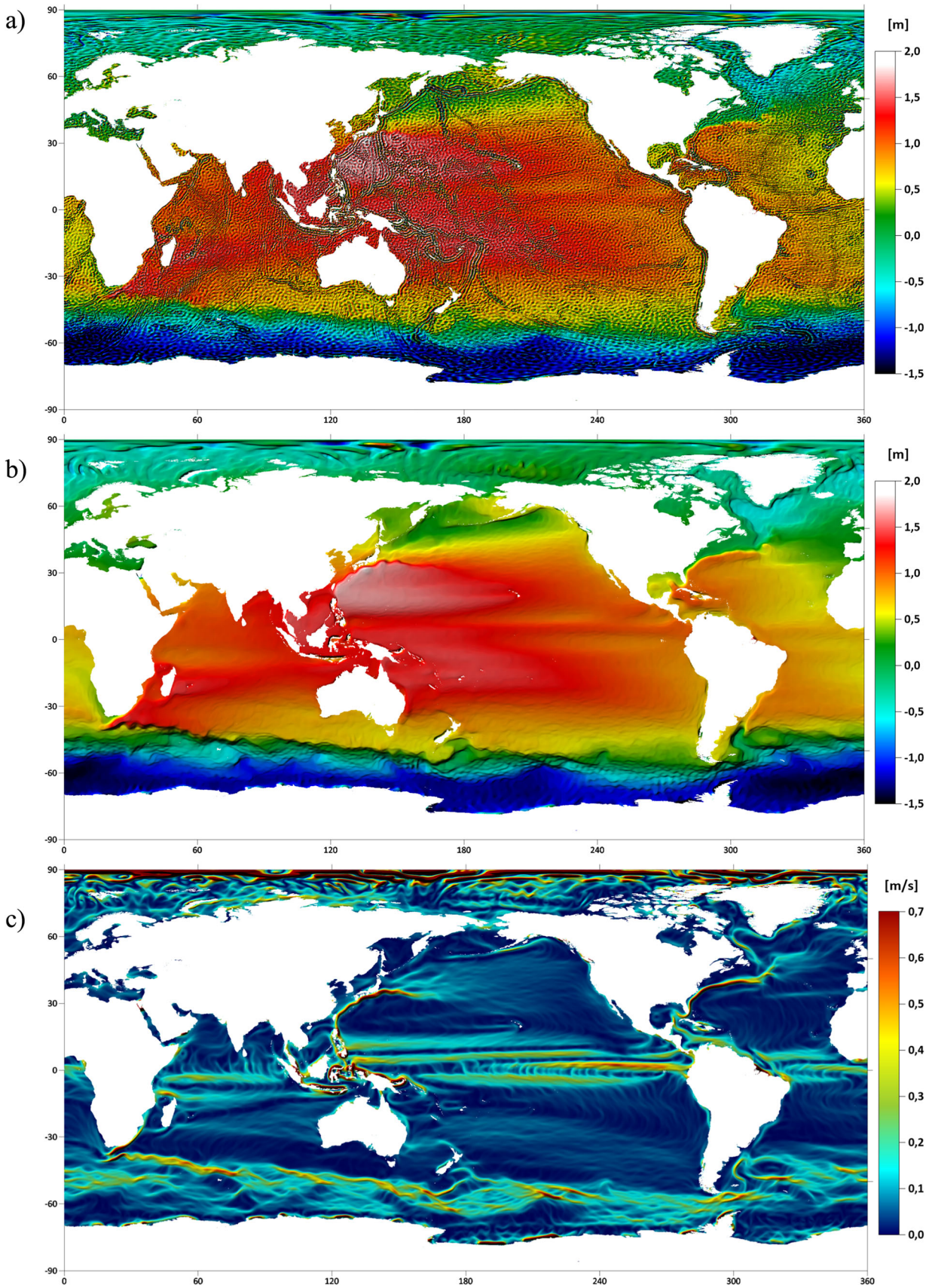

Fig. 4 **a** The satellite-only MDT model as a combination of the DTU21_MSS model and GO_CONS_GCF_2_DIR_R6, **b** the filtered MDT model, and **c** derived velocities of the surface geostrophic currents

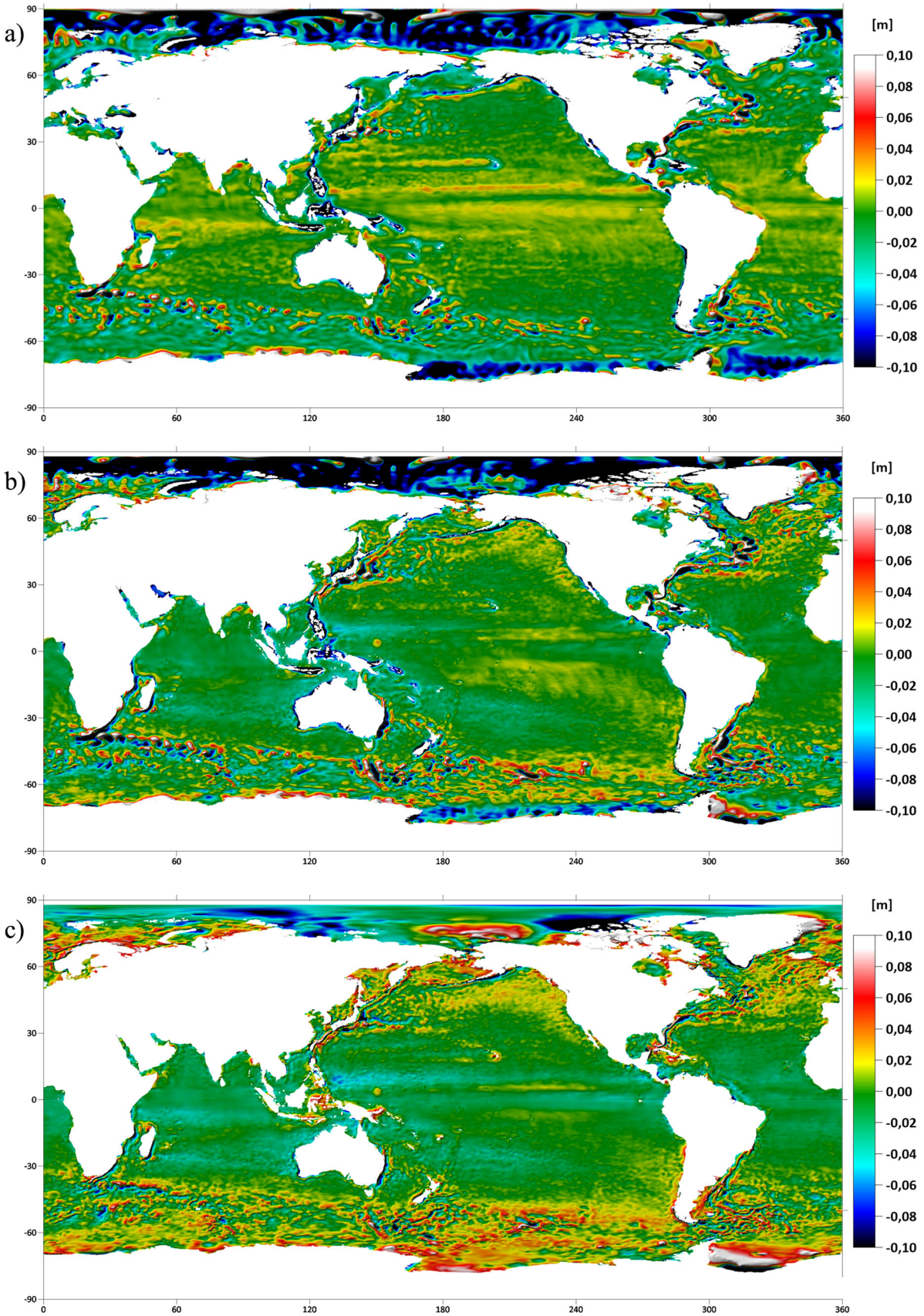

Fig. 5 Comparisons between the MDT models **a** filtered MDT model – DTU22_MDT, **b** filtered MDT model – MDT_CNES_CLS2022, and **c** DTU22_MDT – MDT_CNES_CLS2022

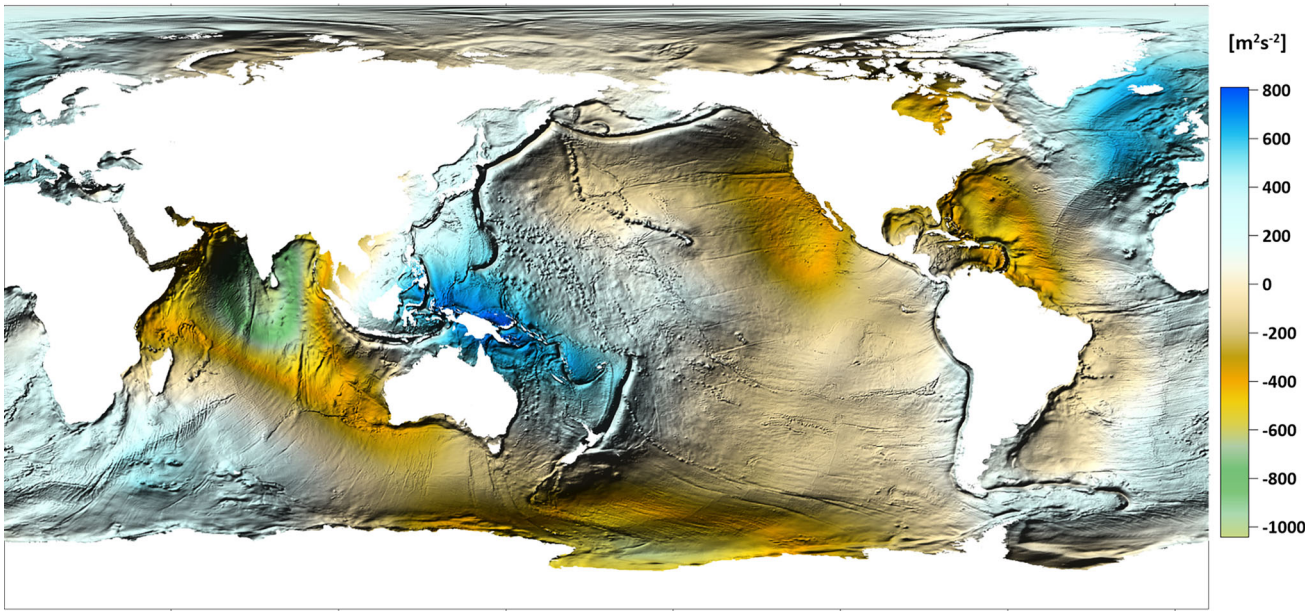

Fig. 6 The disturbing potential over oceans/seas as the Dirichlet boundary condition on the bottom boundary

preserving complicated and very detailed structures of the gravity field.

Figure 7 shows differences between the filtered and original data that apparently represent small and fine noise. Figure 8 depicts a detail in a small area in the Pacific Ocean west of the Mariana Trench, where one can see how the small noise is reduced. Amplitudes of the removed noise are below $\pm$ 0.3 m^2s^{-2} (~ $\pm$ 3 cm) , which is below the declared accuracy of the DTU21_MSS (Andersen et al. 2021).

5 Large-scale parallel computations

A numerical solution of the satellite-fixed AGBVP using the FVM approach (Sect. 2) on the very refined mesh with 93.312 billion of unknowns (Sect. 3) together with incorporating all BCs (Sect. 4) led to very large-scale parallel computations. Therefore, the domain decomposition method, namely the additive Schwarz method with 40 subdomains (Macák et al. 2021), was applied to enormously reduce the memory requirement from about 4.9 TB to approximately only 1 GB. It reduced memory requirements by 80%, however, in the cost of much higher CPU time consumption.

Final large-scale parallel computations were performed on 6 nodes of our cluster with 192 cores and 1.5 TB of distributed memory (each node consists of four 8-cores processors of the NUMA (Non-Uniform Memory Access) architecture and 256 GB of RAM). To minimize the total CPU time, we have applied a hybrid parallelization and the NUMA optimization using 48 MPI processors, each with 4 OpenMP threads (together 192 cores). On such a configuration, the final large-scale parallel computations took about 720 h (~ 30 days) of the CPU time. Since the speed of convergence varied for different subdomains, the CPU time consumption also varied for different processors/cores. The slowest convergence was in polar regions where the BiCGSTAB linear solver (Barrett et al. 1994) required more iterations to reach a prescribed tolerance. Here, the CPU time was almost 1.5 times higher than for the rest of subdomains. This significantly prolonged the total CPU time.

It is also worth mentioning that newest nodes of our cluster performed computations almost 2.5 faster than the oldest ones. In other words, their CPU time consumption was 2.5 times smaller; however, they had to wait for the slowest core in each iteration of the BiCGSTAB linear solver. Consequently, the total CPU time consumption was rather high. Anyhow, we deduce that the same experiment performed on modern clusters or supercomputers at some HPC centre, without a need to apply the domain decomposition, would take less than 7 days. This is quite promising taking into account that such large-scale computations give high-resolution numerical solution not only on the Earth's surface but in the whole 3D computational domain.

6 High-resolution altimetry-derived gravity data as derivatives of the disturbing potential

The large-scale parallel computations resulted in the FVM numerical solution of the satellite-fixed AGBVP in the whole

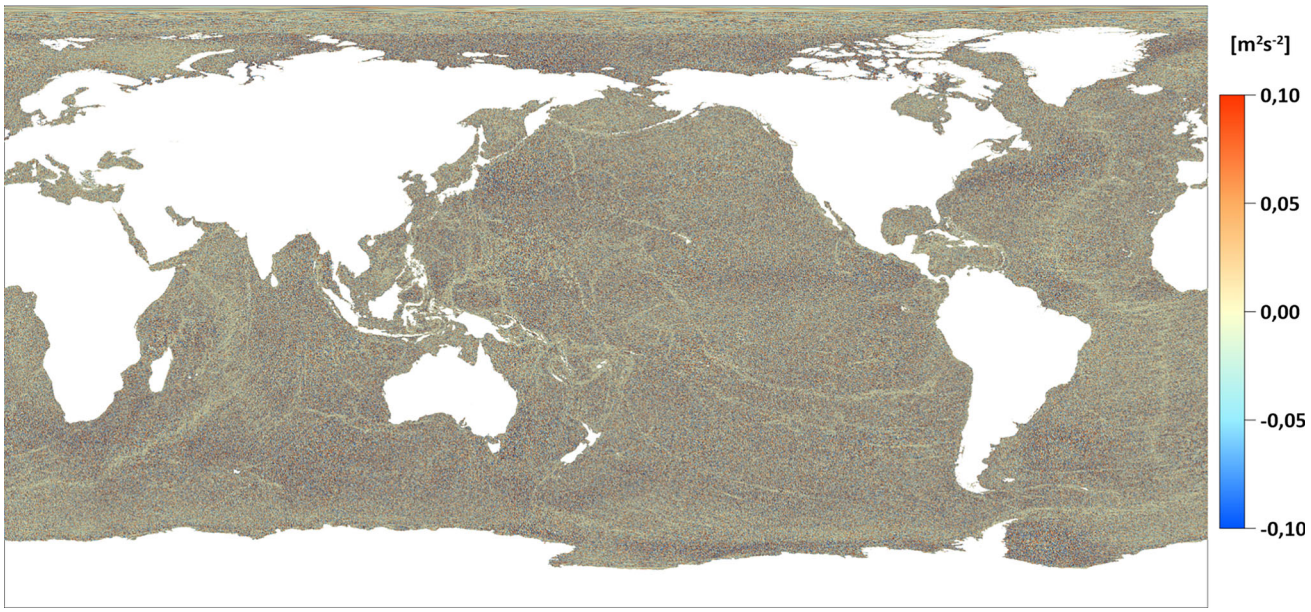

Fig. 7 Differences between the filtered and original disturbing potential evaluated over oceans/seas

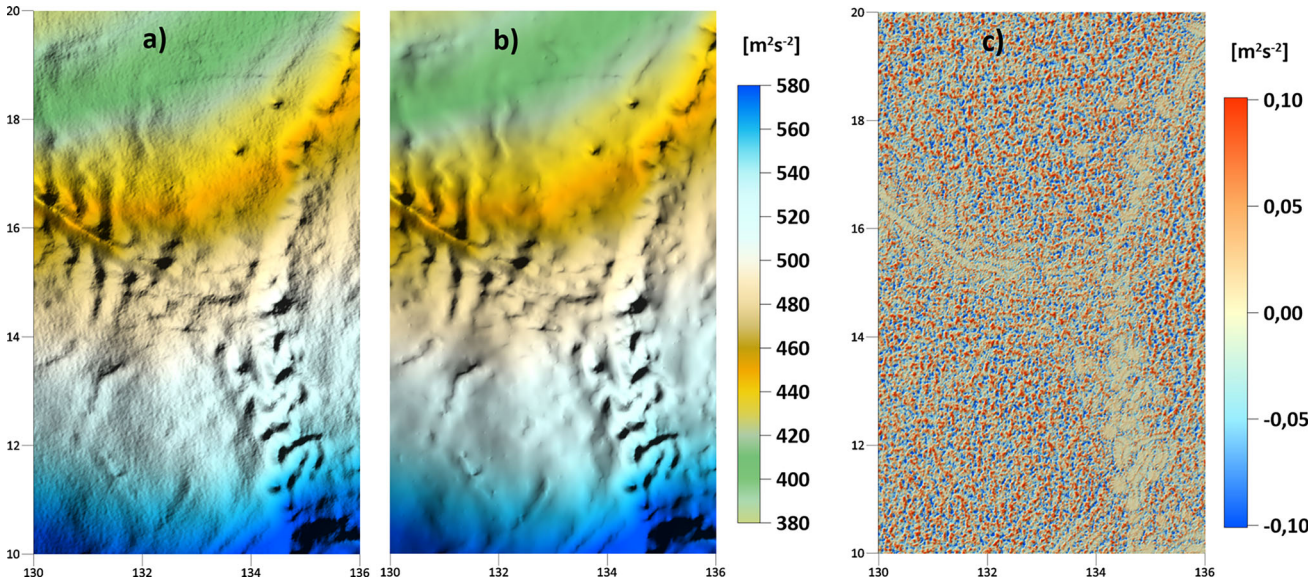

Fig. 8 The detail of the disturbing potential in the Pacific Ocean west of the Mariana Trench: **a** evaluated on DTU21_MSS, **b** filtered by nonlinear filtering, and **c** their differences

3D computational domain between the reference ellipsoid and the upper boundary at the altitude of 200 km. This numerical solution is of the high-resolution 1 × 1 arc min in the horizontal directions. In the radial direction, the non-uniform resolution varies from 50 m close to the ellipsoid up to 960 m at altitude of 200 km (see Sect. 3). It means that the disturbing potential is obtained in every finite volume, from which the first, second or higher derivatives can be numerically derived in different directions using the finite differences.

To get the radial derivatives on the bottom boundary, i.e. on the reference ellipsoid, we use the 4-point forward differences with a uniform grid spacing (see Fornberg 1988)

$$T_Z^{(0m)} = \left(-\frac{11}{6}T^{(0m)} + 3T^{(50m)} - \frac{3}{2}T^{(100m)} + \frac{1}{3}T^{(150m)}\right) \Big/ dh, \tag{7}$$

$$T_{ZZ}^{(0m)} = \left(+2T^{(0m)} - 5T^{(50m)} + 4T^{(100m)} - T^{(150m)}\right) \Big/ dh^2, \tag{8}$$

$$T_{ZZZ}^{(0m)} = \left(-T^{(0m)} + 3T^{(50m)} - 3T^{(100m)} + T^{(150m)}\right) \Big/ \mathrm{d}h^3, \tag{9}$$

where $dh = 50$ m is the radial size of the finite volumes and $T^{(\cdot\, m)}$ is the disturbing potential obtained at the specified heights of the same horizontal coordinates. Hence, T_Z, T_{ZZ} and T_{ZZZ} are of the 3rd, 2nd and 1st order of accuracy, respectively.

To obtain the horizontal derivatives, we use the 5-point central differences with a uniform grid spacing, e.g. in the meridian direction

$$T_X^{(i)} = \left(+\frac{1}{12}T^{(i-2)} - \frac{2}{3}T^{(i-1)} + \frac{2}{3}T^{(i+1)} - \frac{1}{12}T^{(i+2)}\right) \Big/ d\phi, \tag{10}$$

$$T_{XX}^{(i)} = \left(-\frac{1}{12}T^{(i-2)} + \frac{4}{3}T^{(i-1)} - \frac{5}{12}T^{(i)} + \frac{4}{3}T^{(i+1)} - \frac{1}{12}T^{(i+2)}\right) \Big/ d\phi^2, \tag{11}$$

$$T_{XXX}^{(i)} = \left(-\frac{1}{2}T^{(i-2)} + T^{(i-1)} - T^{(i+1)} + \frac{1}{2}T^{(i+2)}\right) \Big/ d\phi^3, \tag{12}$$

where $d\varphi = 1$ arc min is the meridian size of the finite volumes that needs to be transformed into metric units. $T^{(i)}$ represents the disturbing potential in the central point of evaluation, while $T^{(i-1)}$ and $T^{(i+1)}$ are the values in its neighbours along the meridian. Accordingly, T_X, T_{XX} and T_{XXX} are of the 4th, 4th and 2nd order of accuracy, respectively (see Fornberg 1988). Analogously we obtain T_Y, T_{YY} and T_{YYY} while considering the longitudinal size of the finite volumes $d\lambda =$ 1 arc min and corresponding neighbours along the parallel of latitude.

To store all variables at all altitudes would require enormous memory requirements (each variable with the horizontal resolution 1 × 1 arc min takes about 2 GB of memory). Therefore, we decided to store just the disturbing potential in selected altitudes, from which we can evaluate different derivatives anytime if necessary. To derive the radial derivatives at a chosen altitude, we use the 3-point central difference with a non-uniform grid spacing

$$T_Z^{(h_i)} = \frac{1}{2}\frac{\left(T^{(h_i)} - T^{(h_{i-1})}\right)}{(h_i - h_{i-1})} + \frac{1}{2}\frac{\left(T^{(h_{i+1})} - T^{(h_i)}\right)}{(h_{i+1} - h_i)}, \tag{13}$$

where h_i is the altitude of the computational point, h_{i-1} is the altitude of its neighbour below and h_{i+1} of its neighbour above (all 3 points have the same horizontal coordinates). Analogously, the higher radial derivatives can be obtained using the same central difference from the previously evaluated radial derivatives, i.e.

$$T_{ZZ}^{(h_i)} = \frac{1}{2}\frac{\left(T_Z^{(h_i)} - T_Z^{(h_{i-1})}\right)}{(h_i - h_{i-1})} + \frac{1}{2}\frac{\left(T_Z^{(h_{i+1})} - T_Z^{(h_i)}\right)}{(h_{i+1} - h_i)}, \tag{14}$$

$$T_{ZZZ}^{(h_i)} = \frac{1}{2}\frac{\left(T_{ZZ}^{(h_i)} - T_{ZZ}^{(h_{i-1})}\right)}{(h_i - h_{i-1})} + \frac{1}{2}\frac{\left(T_{ZZ}^{(h_{i+1})} - T_{ZZ}^{(h_i)}\right)}{(h_{i+1} - h_i)}, \tag{15}$$

To get horizontal derivatives at any altitudes, we can use the same central differences as described in Eqs. (10)–(12).

6.1 Altimetry-derived marine gravity data on a mean sea surface

The Dirichlet BC over oceans/seas as the crucial input data is considered on DTU21_MSS, although the bottom boundary is approximated by the ellipsoidal approximation of the Earth's surface (Sect. 4). Consequently, the altimetry-derived marine gravity data obtained on the bottom boundary actually represent values derived on DTU21_MSS. It is due to the fact that the FVM approach must satisfy the Dirichlet BC exactly. On the other hand, any latent noise remained in the disturbing potential after its nonlinear filtering (Sect. 4) is transmitted into the FVM numerical solution obtained on the bottom boundary. This effect is intensified with the increasing order of derived derivatives. At higher altitudes, this impact of the latent noise completely vanishes.

All the presented derivatives are expressed in the LNOF (Local North-Oriented Frame). The first derivatives in the radial direction T_Z represent the gravity disturbances δg. The first derivatives in the horizontal directions T_X and T_Y correspond to components of the deflection of vertical, but they are not transformed into these angle quantities. Hence, the units for all three components of the first derivatives are 'mGal' (1 mGal $= 10^{-5}$ m·s^{-2}). Figure 9 depicts the first derivatives T_X, T_Y and T_Z evaluated on DTU21_MSS in the area of the Mariana Trench in the Pacific Ocean.

In the case of the second derivatives, we have derived all the components T_{XX}, T_{YY}, T_{ZZ}, T_{XY}, T_{XZ} and T_{YZ}. They are expressed in the Eötvös units (1 E $= 10^{-9}$ s^{-2}). Figure 10 shows the second derivatives derived on DTU21_MSS in the same area of the Mariana Trench. We have also derived 'diagonal' components of the third derivatives, i.e. T_{XXX}, T_{YYY} and T_{ZZZ}. They are depicted in Fig. 11 and expressed in the units 10^{-13} m^{-1} s^{-2}.

To validate our results, at first we compare the obtained altimetry-derived gravity disturbances with those generated from the recent datasets provided by the DTU approach and S&S approach, namely from the DTU21_GRAV (Andersen and Knudsen 2020) and SS_v31.1 (Sandwell et al. 2021). Since both datasets provide altimetry-derived gravity anomalies Δg, at first we have transformed them into gravity disturbances δg using the formula:

$$\delta g = \Delta g + 0.3086 N^{EGM}, \tag{16}$$

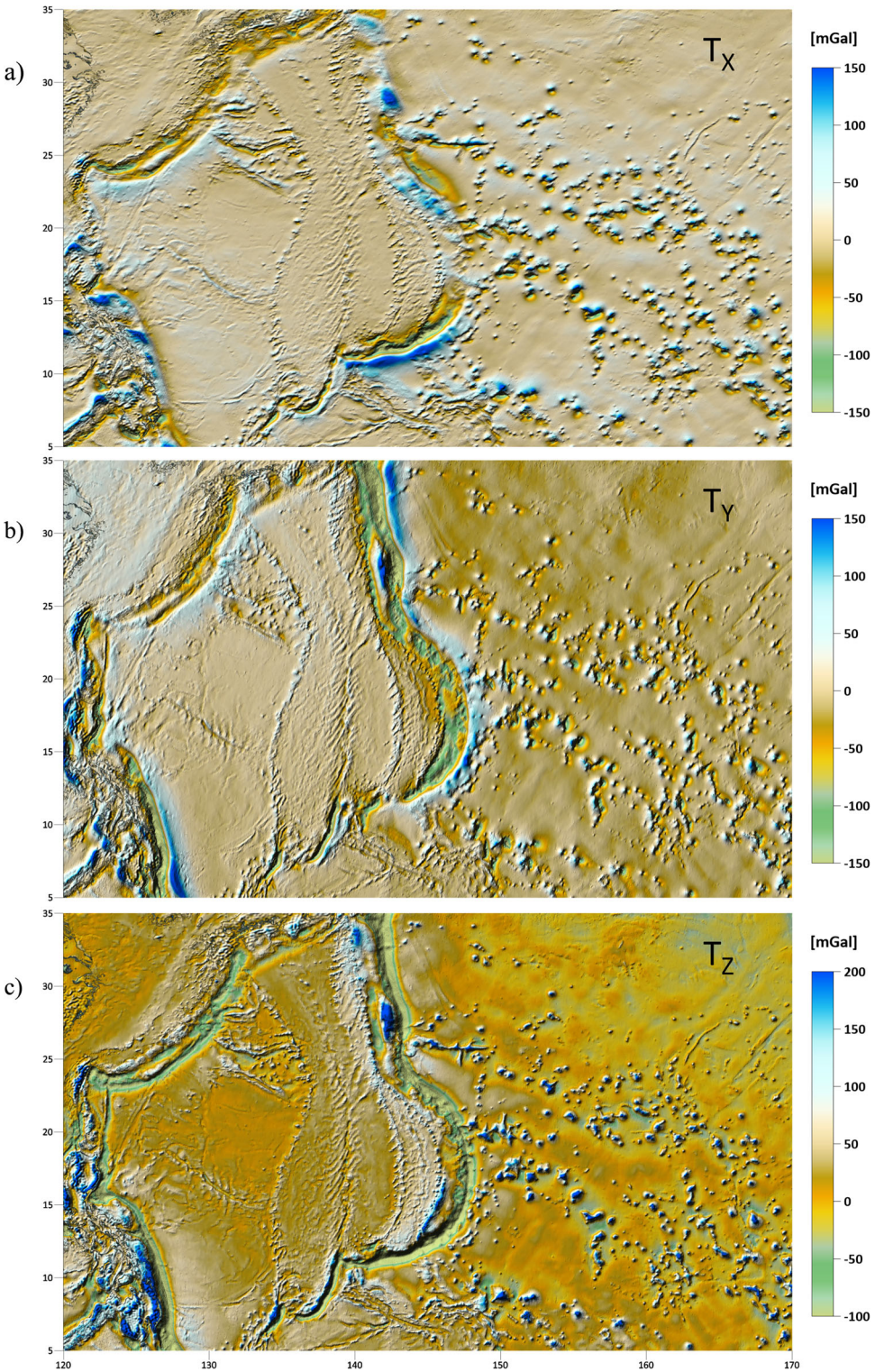

Fig. 9 The first derivatives of the disturbing potential on the DTU21_MSS in the local north-oriented frame

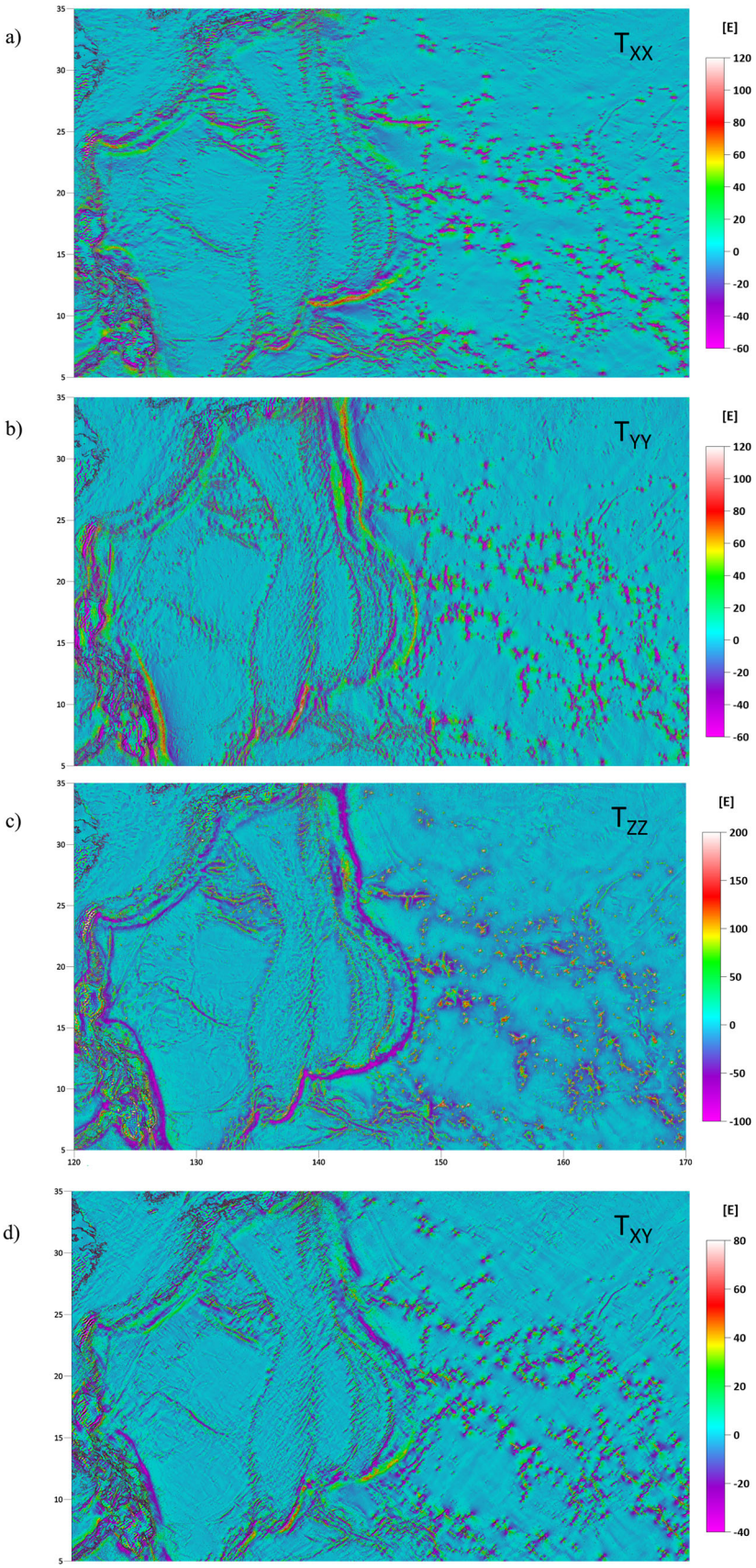

Fig. 10 The second derivatives of the disturbing potential on the DTU21_MSS in the local north-oriented frame

Fig. 10 continued

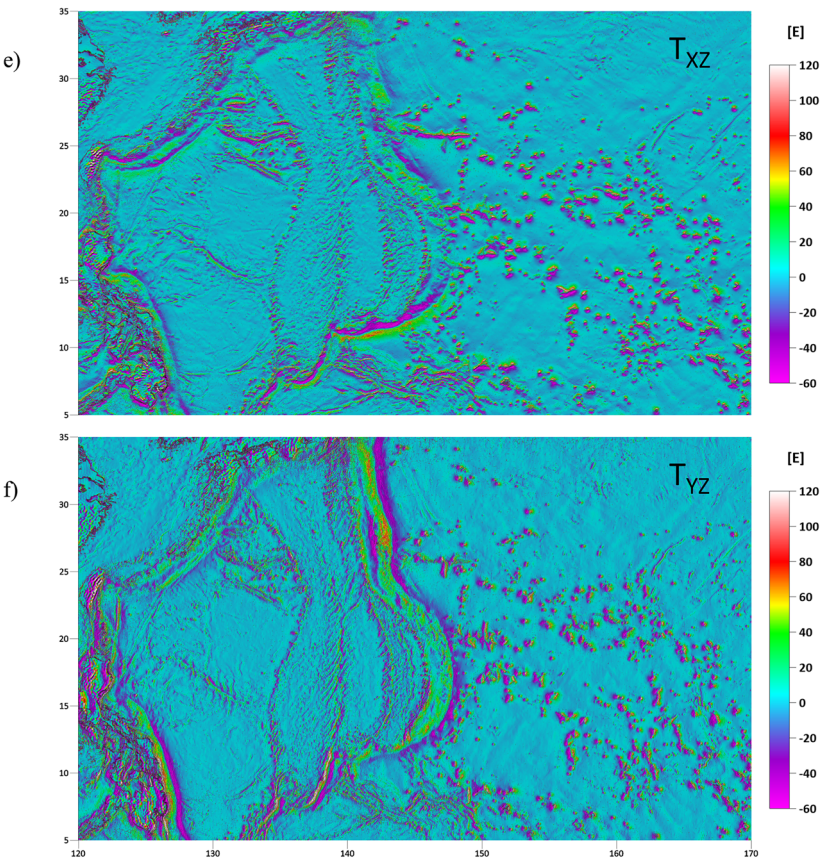

where N^{EGM} is the geoid undulation interpolated from the EGM2008 geoid model (Pavlis et al. 2012). Figure 12 depicts the residuals between the altimetry-derived gravity disturbances over all oceans/seas, and Fig. 13 shows their detail in the North Atlantic Ocean. Table 1 presents statistics of the residuals.

It is evident that the obtained altimetry-derived gravity disturbances better fit to those from DTU21_GRAV. It is logical since both are derived from the same MSS model. In the 'central zone' between the latitudes ⟨-60°,60°⟩, the mean value of residuals is 0.21 mGal for DTU21_GRAV and 0.31 mGal for SS_v31.1, and their standard deviation (StD) is 2.62 and 2.78 mGal, respectively. The largest residuals are obviously at polar zones where StD is higher, in the Arctic Ocean reaching almost 4 mGal (Table 1). This is probably due to a different consideration of MDT in polar regions, which is indicated by high residuals in these zones in Fig. 5a or b. Remark: outliers exceeding ± 50 mGal have been removed from the presented statistics since the most of them are located along coastlines where the different type of BC can cause an undesired jump in the FVM numerical solution.

Figures 12, 13 clearly show that the residuals in the 'central zone' are higher (i) along the main surface geostrophic currents, (ii) along coastlines, and (iii) in zones of fine and sharp structures in the gravity field. The first issue is due to a different consideration of MDT. While the DTU21_GRAV and SS_v31.1 datasets include a-priori information about some MDT model, in our case this is treated by nonlinear filtering of the satellite-only MDT (Sect. 4). For instance, the different residuals along the Gulf Stream in the case of DTU21_GRAV and SS_v31.1 (Fig. 13) nicely demonstrate this different consideration of MDT, see also Fig. 5.

The high residuals along coastlines are partly caused by the aforementioned jump in the FVM numerical solution due to the different type of BC. Here an impact of the DTU15-based input gravity disturbances prescribed on lands/continents as the Neumann BC (Fig. 3) can affect the obtained FVM solution. Moreover, our iterative process of nonlinear filtering of the satellite-only MDT proposed to augment its filtered information to lands (Sect. 4), can also contribute to this inconsistency of input data along coastlines. This can make biases, especially in areas of the high SH-type noise that are indicated by high residuals in some coastal zones in Fig. 5a or b. To reduce such biases, coastal regions would require special treatment based on available local data or information from hybrid MDT models.

The last issue—larger residuals in zones of sharp and fine structures in the gravity field (e.g. over oceanic ridges)—is

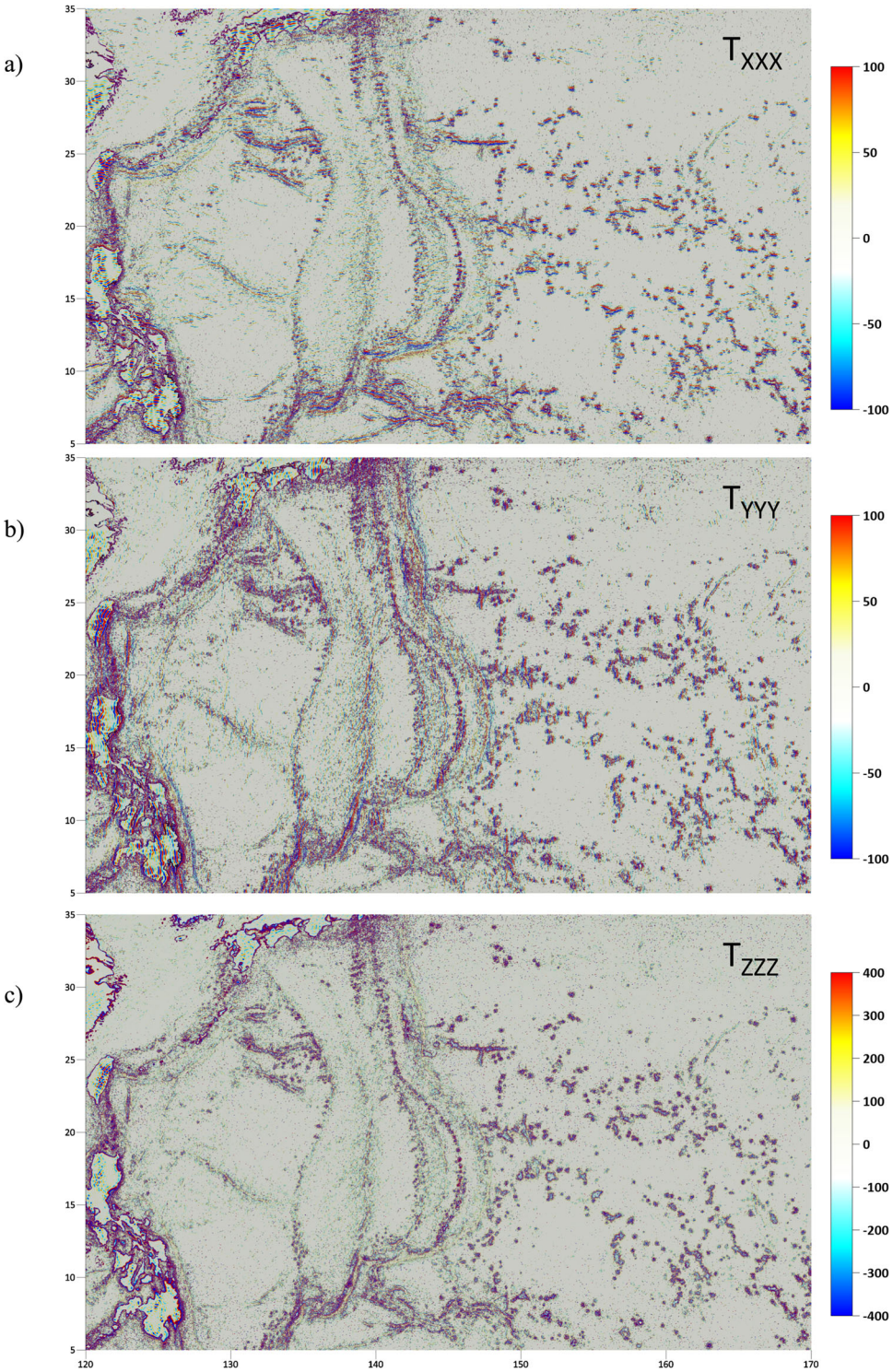

Fig. 11 The third derivatives of the disturbing potential on the DTU21_MSS in the local north-oriented frame (units: 10^{-13} m^{-1} $s.^{-2}$)

probably due to the fact that we use the 4-point forward differences to get radial derivatives on the bottom boundary (see Eqs. 7–9). Consequently, information about the gravity field at points of higher altitudes (50, 100 and 150 m) is naturally slightly smoother. This can make sharp and fine local extremes a little bit smoother because the radial derivatives are derived numerically from all these 4 points. Nevertheless, StD of the residuals below 3 mGal (Table 1) indicates very good matching with the altimetry-derived marine gravity data from DTU21_GRAV or SS_v31.1.

Another assessment of our results is based on their testing by shipborne gravimetry. However, due to large biases

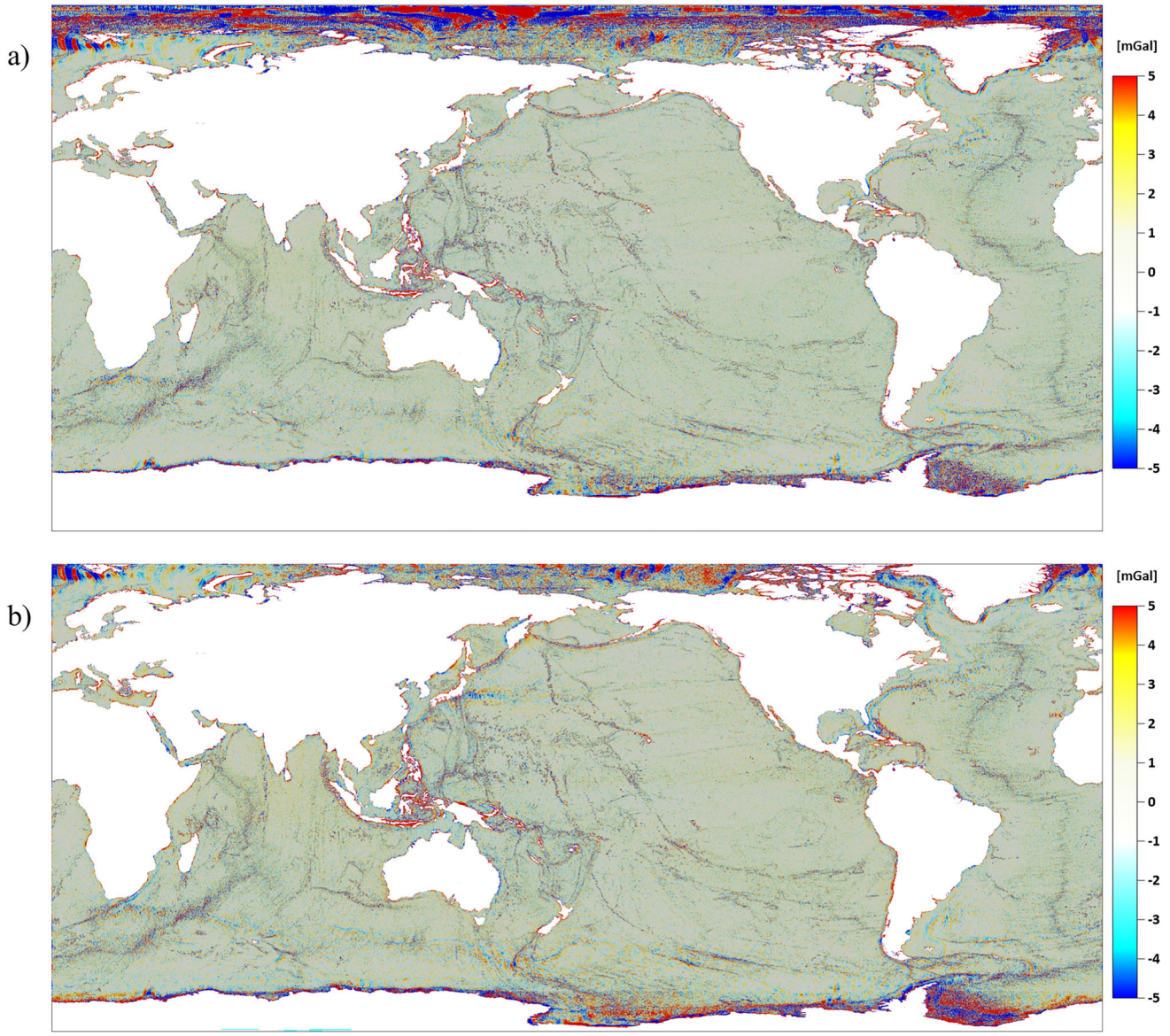

Fig. 12 Residuals between the obtained altimetry-derived gravity disturbances and those generated from **a** the DTU21_GRAV, and **b** SS_v31.1 datasets

and outliers of shipborne gravity data available from BGI (bgi.obs-mip.fr), this test aims to provide only a visual assessment rather than some relevant statistics. Figure 14 depicts residuals between the altimetry-derived gravity data and those from shipborne gravimetry in the area of the Gulf Stream (GS) including the Gulf of Mexico and Antilles. Figure 15 shows such residuals around Greenland. Table 2 presents statistics of the residuals.

The residuals in Fig. 14 show main differences along the Gulf Stream. The best agreement is evidently in the case of DTU21_GRAV for which StD is 2.82 mGal (Table 2). Then, the FVM solution fits slightly better than SS_v31.1; however, it has strong negative residuals close to the east coast of Florida. They are probably due to the aforementioned problem of augmenting MDT data into lands during the process of nonlinear filtering of the satellite-only MDT. Consequently, StDs are very similar, i.e. 3.69 and 3.72 mGal, respectively.

In the Gulf of Mexico, the behaviour of the residuals is very similar for all three cases and StDs vary between 2.33 and 2.55 mGal (Table 2). Negative values dominate in its northeast corner and positive values in its southern part (Fig. 14). It is probably a drawback of the biased shipborne gravity data. Much higher differences are in the area of the Greater Antilles, especially in the zone between Cuba, Jamaica and Haiti. Here the FVM solution, namely its filtered satellite-only MDT model, is strongly affected by complicated structures in the gravity field. The SH-type noise in this

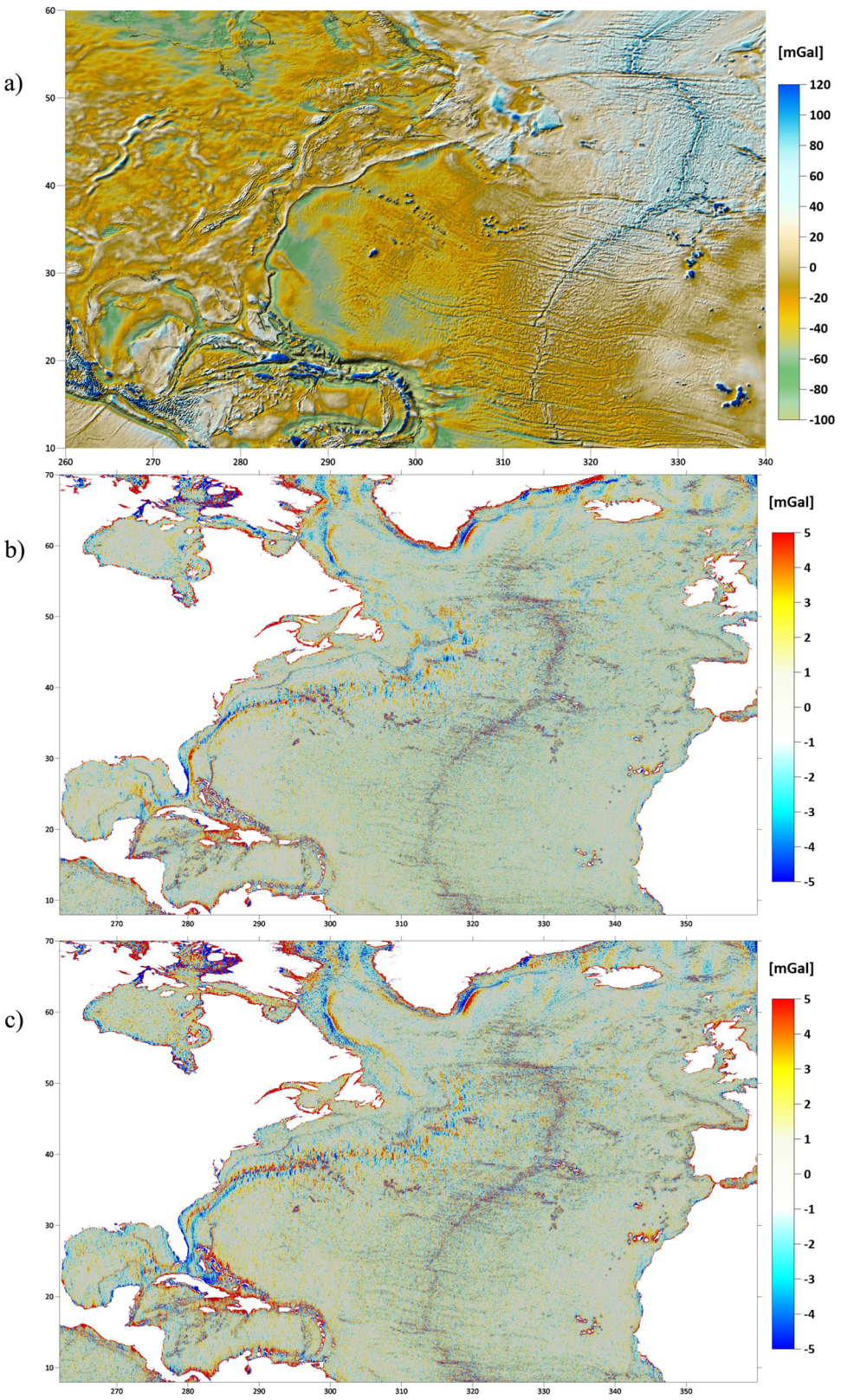

Fig. 13 The detail in the North Atlantic Ocean: a) the obtained altimetry-derived gravity disturbances and their residuals with b) the DTU21_GRAV, and c) SS_v31.1

Table 1 Statistics of residuals between the obtained altimetry-derived gravity disturbances and those generated from the DTU21_GRAV and SS_v31.1 datasets (outliers exceeding ± 50 mGal have been removed)

Area	Residuals: (FVM—dataset) [mGal]							
	DTU21_GRAV				SS_v31.1			
	Latitudes	Points	Mean	StD	Latitudes	Points	Mean	StD
Whole	⟨ − 90°,90°⟩	152,255,910	0.22	2.70	⟨ − 80°,80°⟩	140,510,107	0.32	2.87
Central	⟨ − 60°,60°⟩	113,175,786	0.21	2.62	⟨ − 60°,60°⟩	113,165,463	0.31	2.78
Arctic	⟨ 60°,90°⟩	24,323,524	0.49	3.77	⟨ 60°,80°⟩	12,596,505	0.69	3.98
Antarctic	⟨ − 90°, − 60°⟩	14,756,600	0.12	2.98	⟨ − 80°, − 60°⟩	14,748,139	0.23	3.41

area is reaching several dm which has negatively influenced the process of augmenting MDT data. Consequently, there are zones of strong positive residuals closed to coastlines. To overcome this problem, a local treatment based on information from some hybrid MDT models should be applied.

In the area of the Labrador Current along the coast of Labrador Peninsula (Fig. 15), the agreement is similar for the FVM solution and DTU21_GRAV while SS_v31.1 shows an apparent pattern along this ocean current. It indicates that the a-priori MDT model used for SS_v31.1 is less accurate here. In the case of DTU21_GRAV, there is a zone of significant negative residuals east of the Cumberland Peninsula of Baffin Island. Here the FVM solution fits slightly better. On the other hand, the FVM solution is evidently worse in the Baffin Bay where one can recognize artefacts from the south-north striping noise, probably from the GRACE-based contribution in the satellite-only MDT. It makes zones of strong negative residuals in the area of Lancaster Sound (Fig. 15a). Moreover, the high positive or negative residuals close to coastlines or at narrow bays confirm the aforementioned problem of augmenting MDT data.

6.2 Altimetry-derived marine gravity data at higher altitudes

3D high-resolution modelling allows us to derive also the altimetry-derived marine gravity data at different altitudes. For instance, Fig. 16 depicts the 1st, 2nd and 3rd radial derivatives of the disturbing potential at altitude of 11 km in area of the Gulf of Mexico and Antilles up to Bermuda Islands. The first radial derivatives represent the gravity disturbances that can be compared with gravity data observed by airborne gravimetry.

To validate our results, we compare the obtained altimetry-derived gravity disturbances with gravity data from the GRAV-D airborne gravimetry campaign over US (Youngman et al. 2012). For this purpose, we have interpolated values of our altimetry-derived gravity disturbances at points of the GRAV-D measurements taking into account their precise 3D positions. Figure 17 shows the altimetry-derived gravity disturbances along the CONUS coastlines and over Puerto Rico, and Fig. 18 over Alaska. Both figures also depict their residuals with the GRAV-D gravity data (solely offshore data) and altitudes of the GRAV-D airborne tracks. Table 3 presents statistics of both types of the gravity disturbances as well as of their residuals while divided into several areas.

Looking at this statistics, the mean values vary between ± 2 mGal and StD from 1.63 up to 3.44 mGal (Table 3). Surprisingly, the lowest value 1.63 mGal is in the area of Puerto Rico and Virgin Islands, where the gravity field reaches extremal values. Even at altitude of 11 km, the negative values reach − 314 mGal. Hence, StD of 1.63 mGal in this region of extreme gravity field indicates high accuracy of our results. Analysing the offshore residuals in Figs. 17b and 18b, one can observe slightly biased values along specific airborne tracks, e.g. north-west of Florida or west of Alaska. This could indicate some biases of the airborne gravity data that also affect the statistics in Table 3.

On the other hand, high negative residuals along the east coast of Florida (Fig. 17b), that are also visible in the residuals on the bottom boundary (Fig. 14a), indicate the aforementioned drawback of our FVM solution caused by a process of augmenting MDT data. The same problem of augmenting can cause high positive residuals in several bays of Alaska (Fig. 18b). Nevertheless, StDs of residuals about 3 mGal indicate high accuracy of our altimetry-derived marine gravity data determined also at different altitudes.

7 Discussion and conclusions

The presented altimetry-derived marine gravity data have been obtained as a result of a numerical solution of the altimetry–gravimetry BVP. The FVM approach based on a detailed disretization of the 3D computational domain between the ellipsoidal approximation of the Earth's surface and upper boundary at altitude of 200 km has resulted in 3D high-resolution modelling of the disturbing potential. Afterwards,

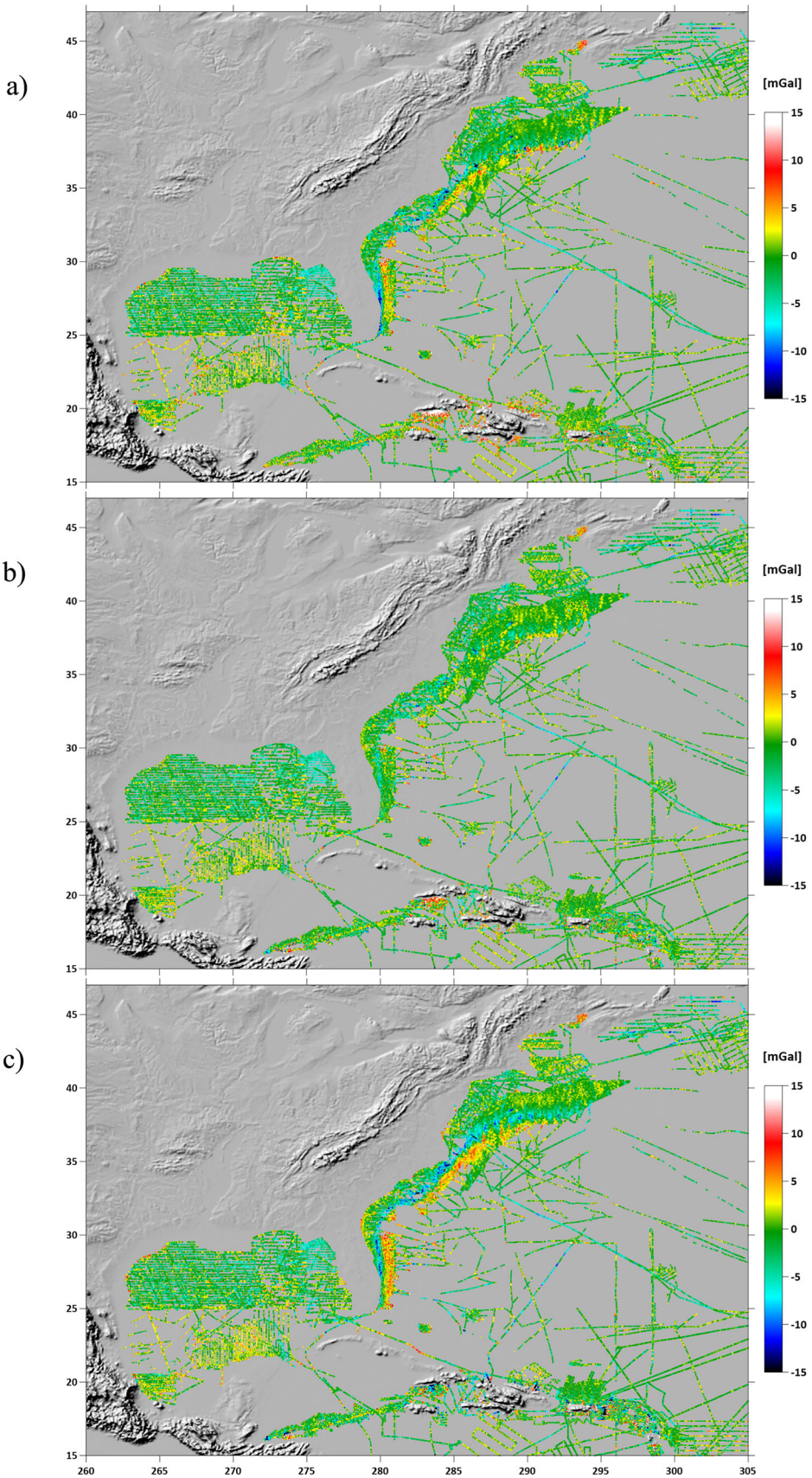

Fig. 14 The altimetry-derived gravity disturbances tested by shipborne gravimetry in the area of the Gulf Stream, Gulf of Mexico and Antilles; **a** the FVM solution, **b** DTU21_GRAV, and **c** SS_v31.1

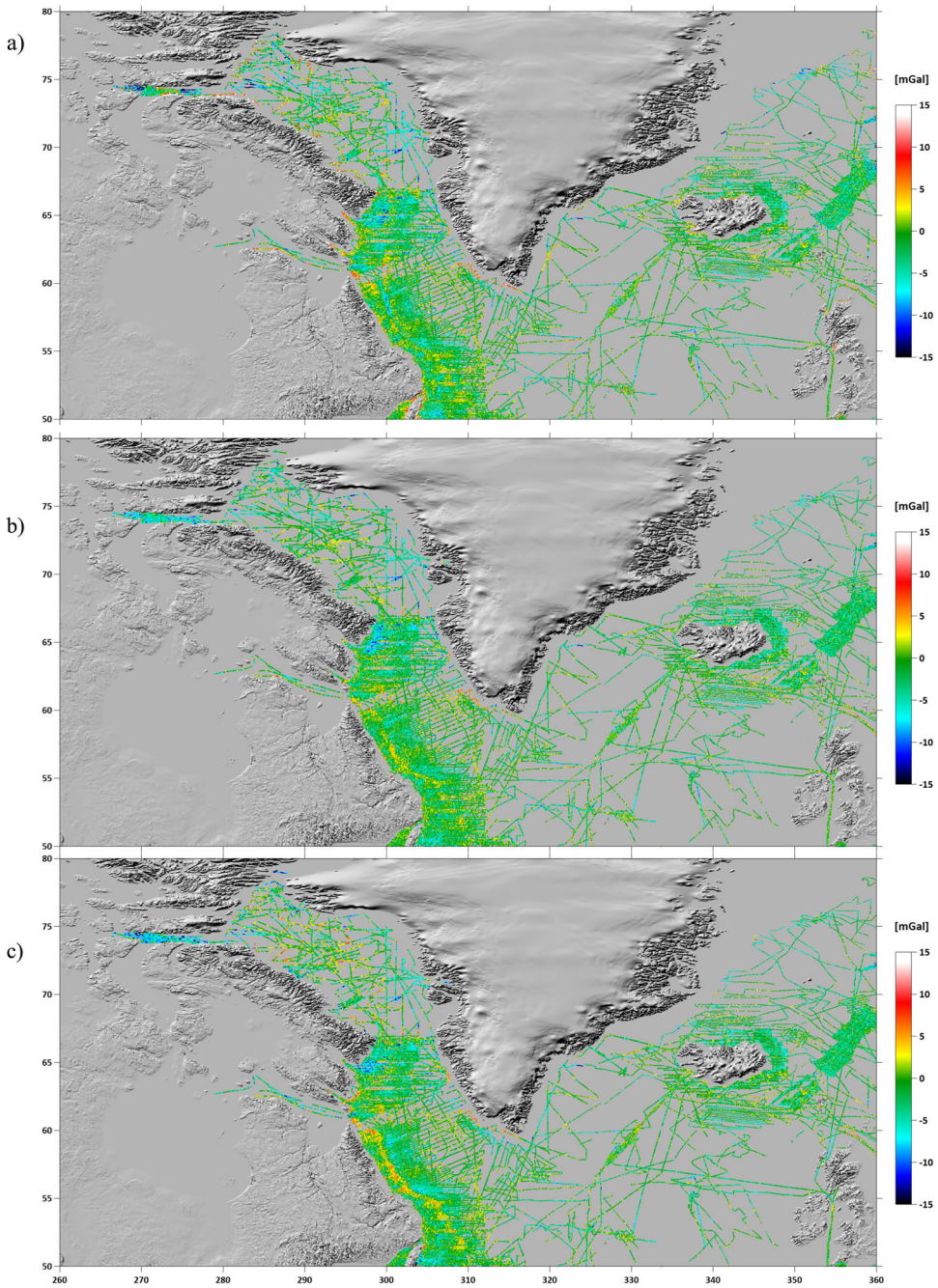

Fig. 15 The altimetry-derived gravity disturbances tested by the shipborne gravimetry around Greenland; **a** the FVM solution, **b** DTU21_GRAV, and **c** SS_v31.1

the first, second or higher derivatives of the disturbing potential in different directions have been numerically derived using the finite differences.

Such an approach conceptually differs from the classical ones used for a compilation of the DTU21_GRAV or SS_v31.1 datasets. At first, the problem is solved numerically in the 3D computational domain what allows us to derive different quantities of the marine gravity field, even at higher altitudes. Secondly, a consideration of the MDT is different. While the DTU approach or S&S approach involves information from a-priori known MDT to get geometrical undulations of the marine geoid, our approach is based on nonlinear filtering of the geopotential generated on a chosen MSS model from some GRACE/GOCE-based satellite-only GGM. In principle, such a treatment also leads to modelling of the satellite-only MDT, which depends on tuning optimal parameters of the nonlinear diffusion filtering; however, it is free of any external MDT model.

On the other hand, our treatment seems to be problematic along coastline zones where the SH-type noise of the satellite-only MDT is reaching high amplitudes. Here the nonlinear filtering, which requires iterative augmenting of

Table 2 Statistics of residuals between the altimetry-derived gravity disturbances and shipborne gravimetry (* data closer than 0.1 deg from coastlines removed)

Area				Residuals: ('altimetry'-'shipborne') [mGal]					
				FVM		DTU21_GRAV		SS_v31.1	
Name	Longitudes	Latitudes	Points	mean	StD	mean	StD	mean	StD
GS—North Atl	⟨278°,305°⟩	⟨23°,47°⟩	330,552	− 0.89	3.69	− 0.81	2.82	− 0.69	3.72
Gulf of Mexico	⟨262°,278°⟩	⟨18°,32°⟩	173,735	− 0.70	2.57	− 0.92	2.33	− 0.85	2.55
Antilles	⟨272°,305°⟩	⟨15°,23°⟩	294,663	+ 0.34	4.44	− 0.30	3.49	− 0.79	4.47
Labrador Curr	⟨295°,317°⟩	⟨50°,67°⟩	610,373	− 1.28	3.18	− 1.46	2.92	− 1.25	3.20
Baffin Bay	⟨265°,308°⟩	⟨67°,79°⟩	129,698	− 1.93	4.57	− 2.63	3.41	− 2.59	4.11
east of Greenland	⟨317°,360°⟩	⟨50°,78°⟩	272,309	− 1.77	3.34	− 1.95	2.90	− 1.79	2.87

the filtered MDT data towards lands (Sect. 4), can lead to biased input data. This drawback has probably caused higher residuals along coastlines, e.g. along the east coast of Florida or around the Great Antilles (Figs. 13 and 14), or in several bays of Alaska (Fig. 18) and Baffin Bay (Fig. 15). To overcome this problem, a local treatment based on information from the hybrid MDT models should be applied.

Nevertheless, a comparison of the altimetry-derived gravity disturbances obtained on the DTU21_MSS with those from the DTU21_GRAV or SS_v31.1 (Table 1, Figs. 12 and 13) and their testing by shipborne gravimetry (Table 2, Figs. 14 and 15) has clearly shown that the presented FVM approach is able to provide marine gravity data of the similar quality. In addition, it can provide all components of the gravity disturbing gradients or higher derivatives with the same 1×1 arc min high-resolution, even at higher altitudes. This is obviously a practical outcome that can be useful for geophysical or geodetic applications.

Testing of the obtained altimetry-derived gravity disturbances at altitudes between 5 and 11 km by the GRAV-D airborne gravity data has indicated accuracy about 3 mGal depending on regions (Table 3, Figs. 17 and 18). Such accuracy is about a level of accuracy of the airborne gravimetry. Depicted residuals enable us to detect tracks with biased airborne gravity data or to identify evident outliers. This confirms high quality of our results. We can assume that other derived quantities like the gravity disturbing gradients or presented diagonal components of the third derivatives are of the same quality.

To improve the quality of our altimetry-derived marine gravity data in the future, we can specify several possibilities. At first, the problematic zones along coastlines should be treated locally. If the SH-type noise of the satellite-only MDT is here too high, it is possible to use information from the hybrid MDT models or to perform the nonlinear filtering of the satellite-only MDT locally by tuning its optimal parameters for these specific regions. Such local tuning of parameters of the edge detector could be also used for regions of main surface geostrophic currents. Indeed, the process of nonlinear filtering plays a crucial role in our approach and has a main impact on accuracy of our results.

Another possibility to improve accuracy of our FVM numerical solution is to increase a level of the discretization of the 3D computational domain. It would yield larger and larger memory requirements, however, nowadays, in the era of the HPC centres with supercomputers and parallel clusters, it is just a question of their accessibility. An opportunity to access such HPC facilities would also allow us to apply the finite element method (FEM) instead of FVM and to solve the AGBVP on the discretized Earth's surface, i.e. directly on a chosen MSS model. In this case, all drawbacks arisen from the ellipsoidal approximation of the Earth's surface will vanish. The FEM approach on non-regular meshes requires about 3.5 times larger memory requirements, cf. Minarechová et al. (2021), but in general, it leads to more precise numerical solutions.

Finally, we would like to emphasize an originality of our results. The altimetry-derived gravity disturbing gradients or the third derivatives that are provided with the high horizontal resolution 1×1 arc min at different altitudes represent an original output. We hope that such detailed gravity data will contribute to a recovery of the global marine gravity field and will be useful for various applications.

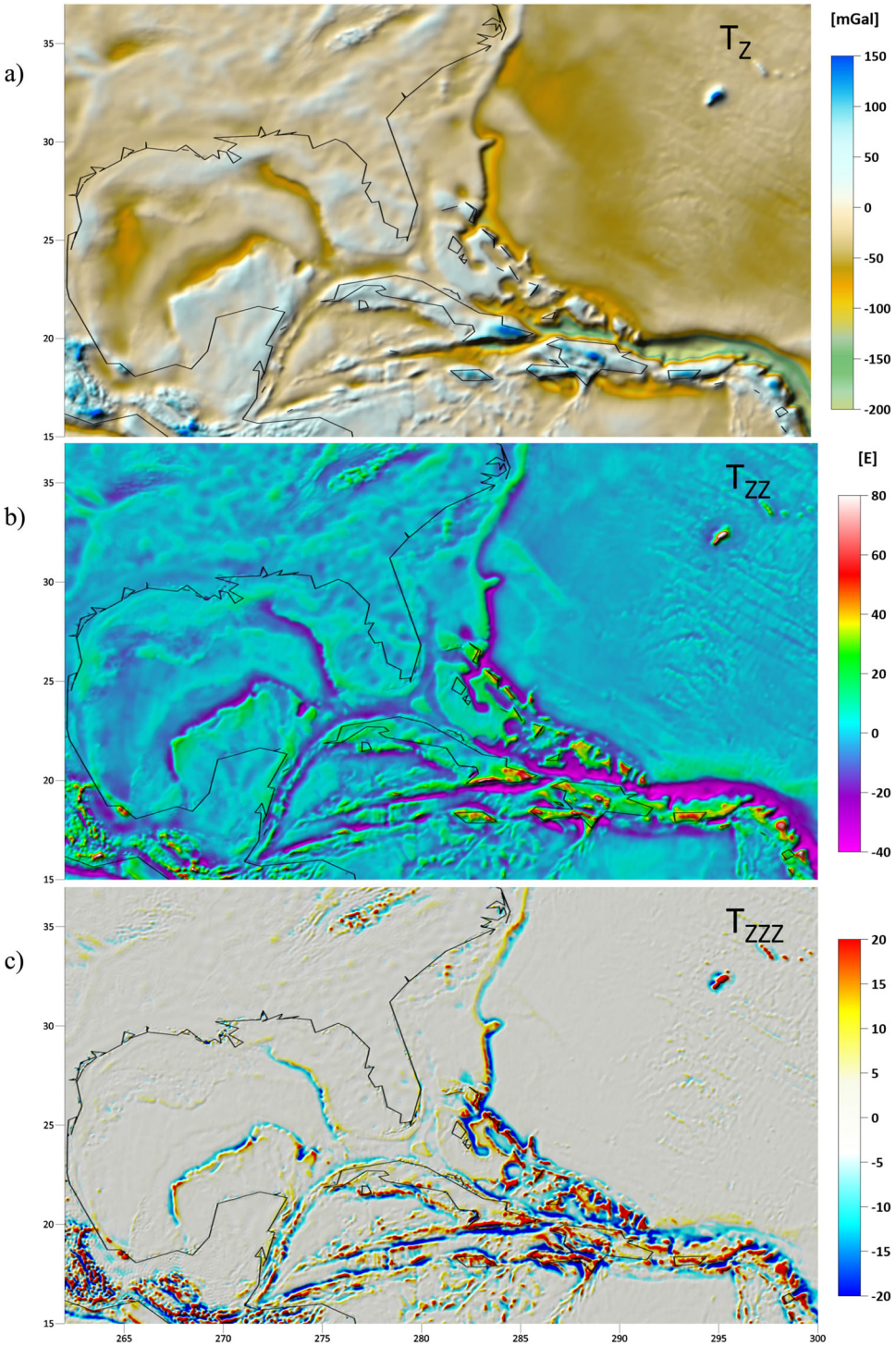

Fig. 16 The 1st, 2nd and 3rd radial derivatives of disturbing potential in the local north-oriented frame at altitude of 11 km

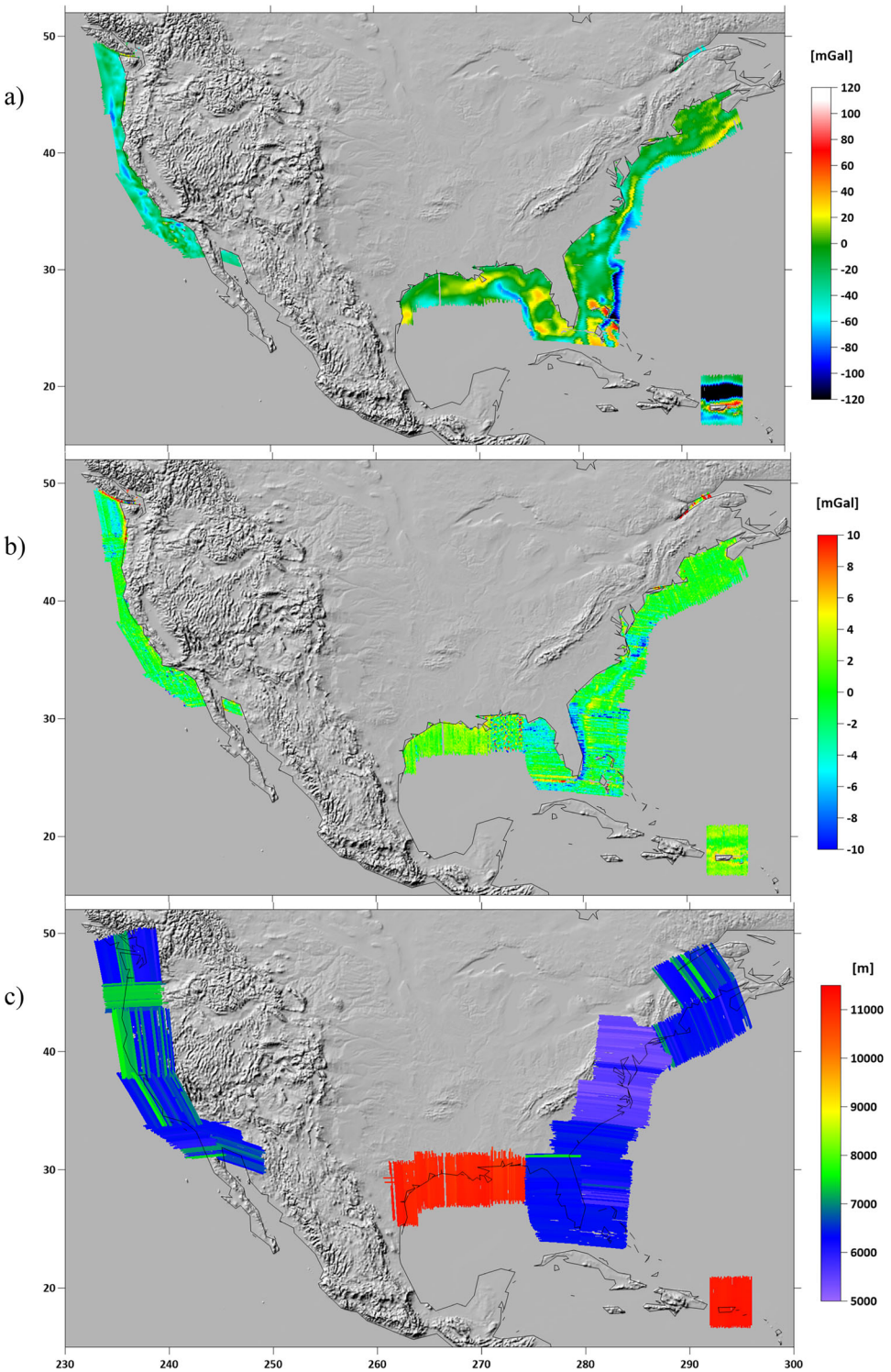

Fig. 17 **a** Altimetry-derived gravity disturbances along coastline areas of CONUS and Puerto Rico, **b** their comparison with the observed values from GRAV-D over oceans/seas, and **c** altitudes of the GRAV-D airborne gravimetry tracks

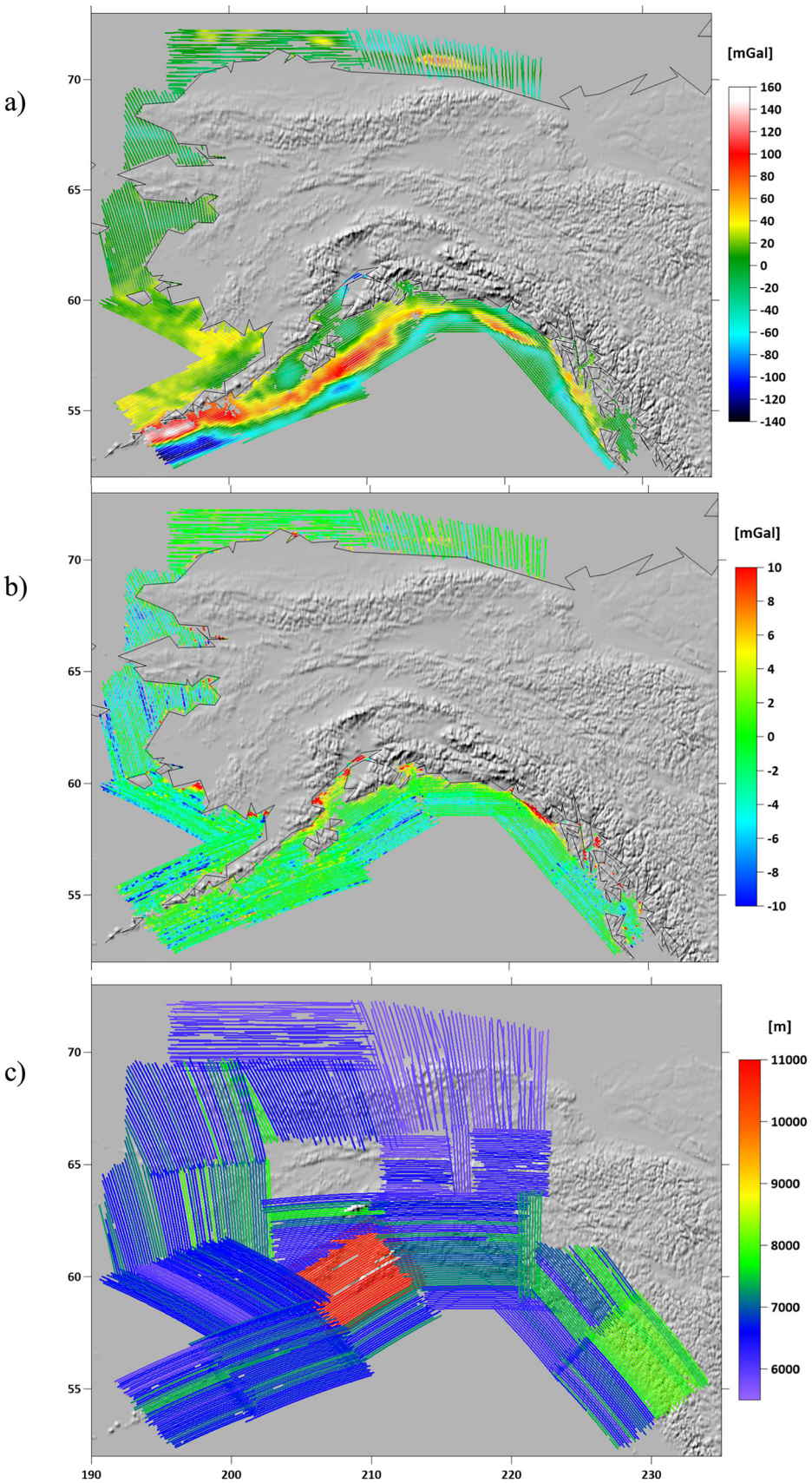

Fig. 18 **a** Altimetry-derived gravity disturbances over Alaska, **b** their comparison with the observed values from GRAV-D over oceans/seas, and **c** altitudes of the GRAV-D airborne gravimetry tracks

Table 3 Statistics of the altimetry-derived gravity disturbances obtained from the FVM solution, gravity disturbances achieved from the GRAV-D airborne gravimetry, and of their residuals (all characteristics considered only for offshore data)

Area	Points	Tracks altitudes [km]		Gravity disturbances [mGal]					Residuals (FVM-GRAV-D) [mGal]			
		Min	Max	Source	Min	Max	Mean	StD	Min	Max	Mean	StD
Alaska	7,936,519	5.5	11.0	FVM	− 134.2	149.1	14.6	48.0	− 49.5	40.6	− 1.59	3.06
				GRAV-D	− 138.9	290.4	16.2	47.7				
West Coast	315,936	5.9	7.6	FVM	− 84.9	27.5	− 35.6	15.6	− 21.2	12.7	− 0.98	2.59
				GRAV-D	− 82.4	37.9	− 34.6	15.3				
East Coast	1,099,792	5.1	7.4	FVM	− 135.2	80.4	− 19.8	25.1	− 19.2	35.4	− 0.89	2.63
				GRAV-D	− 133.0	75.2	− 19.0	24.9				
Gulf of M. (west)	233,461	10.5	11.3	FVM	− 74.8	30.1	− 9.6	21.8	− 37.4	35.1	1.18	3.40
				GRAV-D	− 83.3	43.4	− 10.8	21.6				
Gulf of M.(east)	205,691	6.2	7.4	FVM	− 81.3	47.3	− 2.4	22.8	− 15.5	11.4	− 2.02	2.99
				GRAV-D	− 81.4	52.8	− 0.4	22.7				
Puerto Rico	116,208	11.1	11.3	FVM	− 313.8	74.4	− 86.7	90.9	− 7.5	6.8	2.18	1.63
				GRAV-D	− 314,1	72,7	− 88.8	90.0				

Acknowledgements Funded by the Government of Slovakia through an ESA Contract under the PECS (Plan for European Cooperating States), namely through the PECS contract SK2-08: "GOCE-based high-resolution gravity field modelling in a space domain (GOCE-numerics)". The view expressed herein can in no way be taken to reflect the official opinion of the European Space Agency. This work was also supported by the grants VEGA 1/0486/20 and VEGA 1/0690/24, and the projects APVV-19-0460 and APVV-23-0186. We would like to thank all three anonymous reviewers for their constructive comments and recommendations that helped us to improve our manuscript.

Author contributions RČ proposed the initial ideas, prepared input data, analysed results and wrote the manuscript. MM developed the code and preformed large-scale parallel computations. MK developed and performed nonlinear filtering of input data. ZM and KM proposed and developed numerical approaches. All authors have reviewed and approved the manuscript.

Funding Open access funding provided by The Ministry of Education, Science, Research and Sport of the Slovak Republic in cooperation with Centre for Scientific and Technical Information of the Slovak Republic.

Data availability Data obtained on the mean sea surface are openly available at (www.math.sk/gbvp/data-products/). Due to enormous amount of all output data, those at higher altitudes will be available from the corresponding author upon request.

References

Andersen OB, Abulaitijiang A, Zhang S, Rose SK (2021) A new high resolution Mean Sea Surface (DTU21MSS) for improved sea level monitoring, EGU General Assembly 2021, online, 19–30 Apr 2021, EGU21-16084, https://doi.org/10.5194/egusphere-egu21-16084

Andersen OB, Knudsen P (1998) Global marine gravity field from the ERS-1 and Geosat geodetic mission altimetry. J Geophys Res Oceans 103(C4):8129–8137

Andersen OB, Knudsen P (2016) Deriving the DTU15 Global high resolution marine gravity field from satellite altimetry, In: ESA living planet symposium 2016

Andersen OB, Knudsen P (2020) The DTU17 global marine gravity field: first validation results. IAG Symp 150:83–87. https://doi.org/10.1007/1345_2019_65

Andersen OB, Knudsen P, Berry PA (2010) The DNSC08GRA global marine gravity field from double retracked satellite altimetry. J Geod 84(3):191–199

Andersen OB, Knudsen P, Kenyon S, Holmes S (2014) Global and arctic marine gravity field from recent satellite altimetry (DTU13). In: Presented at the 76th EAGE conference and exhibition 2014, https://doi.org/10.3997/2214-4609.20140897

Barrett R, Berry M, Chan TF, Demmel J, Donato J, Dongarra J, Eijkhout V, Pozo R, Romine C, Van der Vorst H (1994) Templates for the solution of linear systems: building blocks for iterative methods, 2nd edn. SIAM, Philadelphia, PA
http://www.netlib.org/linalg/html_templates/Templates.html

Bjerhammar A, Svensson L (1983) On the geodetic boundary-value problem for a fixed boundary surface - satellite approach. Bull Géod 57:382–393

Bruinsma S, Förste C, Abrikosov O, Lemoine J, Marty J, Mulet S, Rio M, Bonvalot S (2014) ESA's satellite-only gravity field model via the direct approach based on all GOCE data. Geophys Res Lett 41(21):7508–7514. https://doi.org/10.1002/2014GL062045

Čunderlík R, Kollár M, Mikula K (2016) Filters for geodesy data based on linear and nonlinear diffusion. Int J Geomath 7(2):239–274. https://doi.org/10.1007/s13137-016-0087-y

Čunderlík R, Mikula K (2009) Numerical solution of the fixed altimetry-gravimetry BVP using the direct BEM formulation. IAG Symp. https://doi.org/10.1007/978-3-540-85426-5_27
Čunderlík R, Mikula K, Tunega M (2013) Nonlinear diffusion filtering of data on the Earth's surface. J Geod 87(2):143–160
Eymard R, Gallouët T, Herbin R (2000) Finite volume methods. Handbook for numerical analysis 7. Elsevier, Amsterdam, pp 713–1020
Fornberg B (1988) Generation of finite difference formulas on arbitrarily spaced grids. Math Comput 51:699–706
Grebenitcharsky RS, Sideris MG (2005) The compatibility conditions in altimetry-gravimetry boundary value problems. J Geod 78:626–636
Holota P (1980) The altimetry–gravimetry boundary value problem. In: Paper presented at the International Scientific Conference of Sec.6 Intercosmos, Albena, Bulgaria
Holota P (1983a) The altimetry gravimetry boundary value problem I: linearization, Friedrich's inequality. Boll Geod Sci Afini XLII:13–32
Holota P (1983b) The altimetry gravimetry boundary value problem II: weak solution, V-ellipticity. Boll Geod Sci Afini XLII:69–84
Hwang C (1998) Inverse Vening Meinesz formula and deflection-geoid formula: applications to the predictions of gravity and geoid over the South China Sea. J Geod 72:304–312. https://doi.org/10.1007/s001900050169
Hwang C, Parsons B (1996) An optimal procedure for deriving marine gravity from multi-satellite altimetry. Geophys J Int 125:705–718. https://doi.org/10.1111/j.1365-246X.1996.tb06018.x
International Altimetry Team (2021) Altimetry for the future: Building on 25 years of progress. Adv Space Res 68(2):319–363. https://doi.org/10.1016/j.asr.2021.01.022
Jousset S, Mulet S, Wilkin J, Greiner E, Dibarboure G, Picot N (2022) New global Mean Dynamic Topography CNES-CLS-22 combining drifters, hydrological profiles and High Frequency radar data, OSTST 2022, https://doi.org/10.24400/527896/a03-2022.3292
Knudsen P, Andersen OB, Maximenko N, Hafner J (2022) A new combined mean dynamic topography model -DTUUH22MDT. In: Living planet symposium. Bonn, Germany
Lehmann R (1999) Boundary-value problems in the complex world of geodetic measurements. J Geod 73:491–500
Lehmann R (2000) Altimetry-gravimetry problems with free vertical datum. J Geod 74:327–334
Li Q, Bao L, Wang Y (2021) Accuracy evaluation of altimeter-derived gravity field models in offshore and coastal regions of China. Front Earth Sci 9:722019. https://doi.org/10.3389/feart.2021.722019
Li X, Čunderlík R, Macák M, Caccamise DJ II, Minarechová Z, Zahorec P, Papčo J, Roman DR, Krcmaric J, Lin M (2025) Finite volume method: a good match to airborne gravimetry? J Geod 99:4. https://doi.org/10.1007/s00190-024-01922-6
Macák M, Čunderlík R, Mikula K, Minarechová Z (2021) Computational optimization in solving the geodetic boundary value problems. Discrete Contin Dyn Syst S 14(3):987–999. https://doi.org/10.3934/dcdss.2020381
Mather RS (1974) On the solution of the geodetic boundary value problem for the determination of sea surface topography. Geophys J R Astr Soc 39:87–109
Minarechová Z, Macák M, Čunderlík R, Mikula K (2015) High-resolution global gravity field modelling by the finite volume method. Stud Geophys Geod 59:1–20
Minarechová Z, Macák M, Čunderlík R, Mikula K (2021) On the finite element method for solving the oblique derivative boundary value problems and its application in local gravity field modelling. J Geod 95:70
Pavlis NK, Holmes SA, Kenyon SC, Factor JK (2012) The development of the earth gravitational model 2008 (EGM2008). J Geophys Res 117:B04406. https://doi.org/10.1029/2011JB008916
Pujol MI, Schaeffer P, Faugère Y, Raynal M, Dibarboure G, Picot N (2018) Gauging the improvement of recent mean sea surface models: a new approach for identifying and quantifying their errors. J Geophys Res Oceans. https://doi.org/10.1029/2017JC013503
Reddy JN (2006) An introduction to the finite element method, 3rd edn. McGraw-Hill Education, New York
Sacerdote F, Sansó F (1987) Further remarks on the altimetry–gravimetry problems. Bull Geod 61:65–82
Sansó F (1983) A discussion on the altimetry–gravimetry problems. Geodesy in transition. University of Calgary, Calgary, pp 71–107
Sánchez L, Čunderlík R, Dayoub N, Mikula K, Minarechová Z, Šíma Z, Vatrt V, Vojtišková M (2016) A conventional value for the geoid reference potential W0. J Geod 90:815–835. https://doi.org/10.1007/s00190-016-0913-x
Sandwell DT, Harper H, Tozer B, Smith WHF (2021) Gravity field recovery from geodetic altimeter missions. Adv Space Res 68:1059–1072. https://doi.org/10.1016/j.asr.2019.09.011
Sandwell DT, Müller RD, Smith WH, Garcia E, Francis R (2014) New global marine gravity model from CryoSat-2 and Jason-1 reveals buried tectonic structure. Science 346(6205):65–67
Sandwell DT, Smith WHF (1997) Marine gravity anomaly from geosat and ERS 1 satellite altimetry. J Geophys Res 102(B5):10039–10054. https://doi.org/10.1029/96JB03223
Sandwell DT, Smith WHF (2009) Global marine gravity from retracked Geosat and ERS-1 altimetry: Ridge segmentation versus spreading rate. J Geophys Res Solid Earth 114(B1):B01411
Schaeffer P, Pujol MI, Veillard P, Faugere Y, Dagneaux Q, Dibarboure G, Picot N (2023) The CNES CLS 2022 mean sea surface: short wavelength improvements from CryoSat-2 and SARAL/AltiKa high-sampled altimeter data. Remote Sens 15(11):2910. https://doi.org/10.3390/rs15112910
Svensson L (1983) Solution of the altimetry–gravimetry problem. Bull Geod 57:332–353
Youngman M and NOAA's NGS team (2012) GRAV-D Field Operations Handbook. https://geodesy.noaa.gov/GRAV-D/pubs.shtml